STUDIES ON SWELLING RESISTANCE OF PURE CHROMIUM AS A FUEL CLADDING COATING MATERIAL

A Thesis

by

EKATERINA RYABIKOVSKAYA

Submitted to the Office of Graduate and Professional Studies of
Texas A&M University
in partial fulfillment of the requirements for the degree of

MASTER OF SCIENCE

Chair of Committee,	Lin Shao
Committee Members,	Pavel Tsvetkov
	Karim Ahmed
	Kelvin Xie
Head of Department,	Michael Nastasi

December 2020

Major Subject: Nuclear Engineering

ABSTRACT

The Fukushima Daiichi reactor accident showed that Zircaloy-4 fuel cladding tubes under accident conditions involving loss of cooling can lead to strong hydrogen generation and explosion arising from severe surface oxidation of the cladding with water steam. Among various approaches advanced to improve the accident tolerance of fuel pins, coating of the Zircaloy cladding surface is promising, especially if a thin layer of the chosen coating can be minimized to avoid significantly perturbing the neutron economy, thereby allowing the low neutron absorption benefit of Zircaloy-4 cladding to be retained.

One coating candidate, chromium, has good high temperature strength, hardness and wear resistance. Most importantly, chromium can form a thin layer of tenacious chromium oxide on the cladding surface for superior corrosion resistance, which makes it ideal as additional protection on Zircaloy cladding for enhanced accident tolerance under reactor off-normal conditions. Compared to other candidates, chromium has a relatively low neutron absorption cross section but its impact on the neutron economy cannot be completely ignored.

Radiation resistance of any coating deposited on fuel cladding must be as high as zirconium alloy underlayer. Neutron and heavy ion irradiation data as well as void swelling behavior analysis on pure chromium in a form of bulk material or coatings is very limited and still requires additional research efforts.

In the present study, pure chromium was irradiated with 5 MeV Fe^{2+} ions to 50 peak dpa at temperatures of 450, 500, 550, 600 and 650°C. Then irradiation at the peak swelling temperature of 550°C was conducted to 50, 100, 150 peak dpa. The maximum swelling

temperature identified from the present study is much lower than the earlier studies. Swelling of pure chromium at 50 dpa was observed over the entire 450 and 650°C temperature range studied but appeared to be decreasing strongly at the temperature boundaries of the experiment. Chromium swells at a rate of ~0.03-0.04%/dpa, which is much lower than pure Fe. This low swelling rate was found to be relatively insensitive to dpa rate, which varied a factor of ~2 over the depth of data collection. Swelling begins quickly with essentially zero incubation dose but exhibits a much higher transient swelling rate before settling onto the post-transient value. Self-organization in the form of void ordering into was observed to be developing at 50 dpa, becoming better defined with increasing dose. The void alignment direction is determined to be [111] axial direction.

DEDICATION

To my family.

ACKNOWLEDGEMENTS

First of all, I want to thank my research advisor and committee chair Dr. Lin Shao for his help, support and amazing patience throughout my studies and experiments. I want to thank Dr. Garner for his inspiration, passion and scientific courage, his love to my homeland and people.

Also, I would like to thank my committee members, Dr. Tsvetkov, Dr. Xie, and Dr. Ahmed, for their classes, friendly and creative learning environment.

I want to thank my colleagues and especially Aaron French, for his kindness, enormous help, guidance with the equipment and his company during sleepless day and night shifts in the lab.

CONTRIBUTORS AND FUNDING SOURCES

Contributors

This study was supervised by a committee consisting of Professors Lin Shao, Pavel Tsvetkov and Karim Ahmed of the TAMU Department of Nuclear Engineering and Professor Kelvin Xie of the TAMU Department of Material Science and Engineering.

Lab manager Xuemei Wang, and my colleagues, Aaron French and Adam Gabriel, helped me with accelerator operation and beam watching on 3 MV machine.

Another colleague Tianyao Wang helped greatly with EBSD and double tilt TEM imaging.

All other work conducted for this research was completed by me.

Funding sources

The study was funded by US National Science Foundation award Nº1708788.

NOMENCLATURE

AM	Atom Mirny, Russian for "Atoms for Peace"
AMB	Atom Mirny Beloyarsk
ATF	Accident Tolerant Fuel
BCC	Body Centered Cubic
BF	Bright Field
BOR-60	Fast Sodium-Cooled Reactor, Russian for "Fast Experimental Reactor"
BWR	Boiling Water Reactor
CANDU	Canada Deuterium Uranium Reactor
CCD	Charge Coupled Device
CNP	China Nuclear Power
CTE	Coefficient of Thermal Expansion
Cr	Chromium
dpa	displacements per atom
EDS	Energy Dispersive Spectroscopy
EELS	Electron Energy Loss Spectroscopy
EFTEM	Energy Filtered Transmission Electron Microscopy
EGP	Russian for “Energy Heterogeneous Loop Reactor”
EPRI	Electric Power Research Institute
FCC	Face Centered Cubic
Fe	Iron
FIB	Focused Ion Beam

GE	General Electric
Gen IV	Fourth Generation reactors
GIS	Gas Injection System
HCP	Hexagonal Closest Packed
HE	High Energy
IAEA	International Atomic Energy Agency
LE	Low Energy
LWR	Light Water Reactor
MCF	Materials Characterization Facility
MDA	Mitsubishi Developed Alloy
MIC	Microscopy Imaging Center
NDA	New Developed Corrosion Resistant Alloy
NEC	National Electrostatic Corporation
NRX	National Research Experimental Reactor
PCV	Primary Containment Vessel
Pt	Platinum
PWR	Pressurized Water Reactor
RBMK	Soviet-designed high-power channel reactor
RF	Radio frequency
SCC	Stress Corrosion Cracking
SE	Secondary Electron
SEM	Scanning Electron Microscopy
SNICS	Source of Negative Ions by Cesium Sputtering

SRIM	Stopping and Range of Ions in Matter
SS	Stainless Steel
STEM	Scanning Transmission Electron Microscopy
TEM	Transmission Electron Microscopy
VVER	Water-Water Energetic Reactor (WWER)
Zr	Zirconium
ZIRLO	Zirconium Low Oxidation Alloy
ZLP	Zero-Loss Peak

TABLE OF CONTENTS

Page

LIST OF FIGURES

1. INTRODUCTION

According to the IAEA [1], there are 451 operating nuclear reactors and 52 more under construction in the world. These are mostly pressurized water reactors, or PWR (US, France, Japan, China, South Korea, UK, Germany, etc.), and boiling water reactors, or BWR (US, Japan, India, Germany, etc.). Some units (VVER-440 and VVER-1000) are of Russian design. Other designs are channel-type reactors, such as CANDU (Canada, China and South Korea), RBMK-1000 or EGP (Russia). China develops its own design of nuclear reactors (CNP-1000, CNP-600 and CNP-300).

Nuclear fuel comes in the form of fuel assemblies consisting of fuel rods. Fuel rods of light water (thermal neutron) reactors contain uranium dioxide pellets placed inside a cladding tube made of a zirconium alloy. The fuel rod cladding is the first physical barrier preventing fission products from getting into the coolant.

Low neutron absorption cross section along with corrosion resistance, adequate high-temperature mechanical strength, and dimensional stability under radiation made Zirconium alloys the best option for light water reactors fuel cladding and core internals. Zr-alloys have preference over stainless steels because they help to reduce the required fuel pellet enrichment and increase fuel discharge burnup. [2]

The nuclear industry has several well-proven zirconium-based alloys for LWR fuel assemblies; the most common alloys are presented in the Table 1.1.

Among common Zr-alloys are Russian-designed alloys E110 (fuel cladding, plugs and spacer grids), E635 (pressure tubes and fuel assembly stiffeners), and E125 (RBMK pressure tubes). Alloys designed for similar purposes in the USA and Canada are Zircaloy-

2 (Zry2), Zircaloy-4 (Zry4) and Zr2.5Nb. Zirconium alloys keep improving, with compositions becoming more complex – zirconium is combined with niobium, tin, iron and oxygen (E635, ZIRLO, etc.).

Table 1.1 Cladding Alloy Compositions (in wt% Unless Specified in Weight Parts per Million, wppm).

Alloy	Sn	Fe	Cr	Nb	Ni	O	C	Other
Zircaloy-2 (ASTM B811)	1.2–1.7	0.07–0.2	0.05–0.15	–	0.03–0.08	0.09–0.16	0.027 Max	
Zircaloy-4 (ASTM B811)	1.2–1.7	0.18–0.24	0.07–0.13	–	–	0.09–0.16	0.027 Max	
ZIRLO (Nominal)	1	0.1	–	1	–	1250 wppm		
M5 (Nominal)	–	150–600 wppm	–	1		900–1800 wppm	25–120 wppm	S: 0–35 wppm
E110 (Nominal)	–	0.006–0.012		0.95–1.05	30–60 wppm	500–700 wppm	50–100 wppm	
Optimized ZIRLO	0.67	0.1	–	1		1250 wppm		

Unfortunately, the history of the nuclear power industry knows several severe meltdown accidents. In December 1952, the core of the NRX reactor at Chalk River Laboratories [3] in the Canadian province of Ontario was overheated, resulting in a partial meltdown. In 1979, an accident at the Three Mile Island Nuclear Generating Station in Pennsylvania (USA) [4] resulted in 53% of the reactor core melted down. Then came the Chernobyl disaster [5] – the reactor core at Unit 4 was destroyed.

On 11 March 2011, the tsunami following a strong earthquake caused a loss-of-coolant accident and a meltdown at Unit 1 of the Fukushima Daiichi Nuclear Power Plant in Japan [6]. According to World Nuclear Association [7] Units 1-3 at Fukushima Daiichi lost

power about an hour after the quake, when the entire site was flooded by the 15-metre tsunami. Tsunami disabled back-up generators on site and the heat exchangers for dumping reactor waste heat and decay heat to the sea. All three units lost the ability to maintain proper reactor cooling and water circulation functions. After shutdown without heat removal by circulation to an outside heat exchanger reactor cores would still be producing about 1.5% of their nominal thermal power, that produced a lot of steam in the reactor pressure vessels housing the cores. Steam was released into the dry primary containment (PCV) through safety valves. Later this was accompanied by hydrogen, produced by the interaction of the fuel's very hot zirconium cladding with steam after the water level dropped. As a result, major fuel melting occurred in all three units.

When inside the core, fuel assembly components made of zirconium alloys develop a thick zirconium oxide film, which is an effective barrier protecting the alloy from oxygen and hydrogen. What happens when LWR fuel claddings are overheated? As temperature grows, phase changes in zirconium and its oxide cause protective properties of zirconium oxide to degrade. This process is also contributed to by the swelling of the cladding under the pressure of high temperature produced gases from inside, which leads to decomposition of the oxide [8].

As a chemically active element, zirconium starts interacting with water steam. When temperature exceeds 900°C, an exothermic reaction begins, with much energy (around 600 kJ/mole) and a large amount of hydrogen released.

$$Zr + 2H_2O = ZrO_2 + 2H_2$$

As a result, the cladding absorbs oxygen and hydrogen and embrittles. The oxidation process is so intensive that the fuel cladding can break apart.

During severe LOCA accidents, like the one at Fukushima Daiichi, core cooling is interrupted, and the core temperature is driven upward by the decay heat in the fuel [31]. What happens if the core loses its cover due to decrease of water level? First, the heat transfer goes down, core temperature rises, and the fuel elements experience physical and chemical degradation. Around 700–1000°C physical degradation occurs and as temperature goes up - chemical degradation.

Chemical degradation mostly caused by steam oxidation of zirconium. For example, each PWR fuel assembly has about 125 kg of Zr metal and can produce more than 820 MJ of heat and 2700 mol of hydrogen gas once it is oxidized. In the LWR core, depending on the design, 25–40 tonnes of zirconium is present, if fully oxidized, that would produce an excessive amount of heat in addition to the decay heat in the fuel [32].

1.1. Accident tolerant fuel development

Accident at Fukushima Daiichi showed that development of a fuel cladding resistant to high temperature oxidation is critical for the safety of nuclear power reactors. In order to map paths to the development of an accident tolerant fuel, it is reasonable to analyze past efforts at selecting materials for fuel claddings of the first nuclear power reactors. The reactors of Obninsk (AM), Beloyarsk (AMB-100 and AMB-200) and Bilibino (EGP-6) nuclear power plants had fuel claddings made of austenitic steel grades. They contained dispersion type fuel elements, i.e. elements in which a fissionable material (uranium or uranium dioxide alloys) was dispersed in non-fissionable alloys of copper, magnesium or other metals [9].

In Western-designed reactors, claddings were also made of austenitic steel and high-nickel alloys. However, these materials have a significant inherent disadvantage: internal

stresses cause the so-called stress corrosion cracking (SCC). For example, out of nearly 200,000 stainless steel claddings operated by Westinghouse, every hundredth cladding developed stress corrosion cracks, resulting in cladding failures [10].

In the 1950s, the first attempts were made to design marine-type reactors. The above described behavior of fuel claddings was unacceptable, and researchers concentrated their efforts on the development of zirconium alloys.

H1 and H2.5 alloys were developed in the USSR, Zry2 and Zry4 in the USA, and Zr2.5Nb in Canada. Irradiation behavior of these alloys was yet to be studied to ensure operational safety of nuclear reactors.

Studies focused on such properties as radiation-induced growth and creep, oxidation in the coolant, and reactions with hydrogen (as a chemically active metal, zirconium easily forms hydrides, resulting in delayed hydride cracking). Research in zirconium alloy improvement has not stopped since the 1960s. The latest developments are E635 alloy in Russia, ZIRLO in the West, NDA and MDA in Japan [30].

As mentioned above, the greatest disadvantage of zirconium alloys is intensive high temperature oxidation of zirconium and accumulation of explosive hydrogen in the reactor core. For safety purposes, oxidation should be reduced to a level at which ductility of the claddings remains sufficient for the core to be disassembled after an accident and fuel assemblies to be safely transported to a disposal site.

Efforts to create a fuel that is more resistant to high temperature oxidation are concentrated in several areas. Conservative approaches focus on two ways of preserving the integrity of zirconium, either by changing its surface structure (phase) to make it more

resistant to corrosion or by developing protective metal, alloy or ceramic composite coatings (Figure 1.1).

A more radical approach is based on replacing zirconium with more accident-tolerant materials, i.e. materials reacting with steam with less energy and hydrogen released. These materials are alloys based on iron, ceramic composites and silicon carbide. Using two- and three-layer claddings could be a promising solution.

Every country that has a nuclear power program has been working hard on the development of an accident tolerant fuel. Each national program provides for short- and long-term measures. Short-term measures (1 to 10 years) include the development of new coatings, while long-term measures are expected to find an alternative to zirconium.

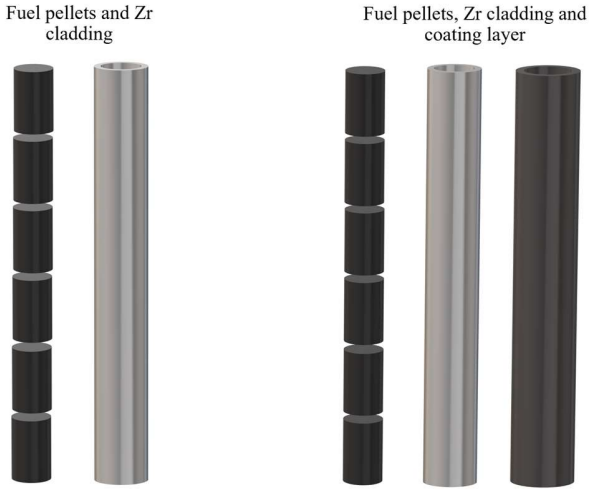

Figure 1.1 Classic Fuel (left) and Accident Tolerant Fuel (right) concepts.

Zirconium is a material prone to deformation. First, it undergoes alpha to beta phase transformation; second, it has an HCP lattice and is therefore prone to radiation-induced growth and, when irradiated for a long time, to radiation-induced creep. It means that the

coating should maintain adhesion to the underlying alloy while the cladding deforms during normal operation. Besides, the coating should be able to slow down the diffusion of oxygen and hydrogen. Its coefficient of thermal expansion (CTE) should be close to CTE of the zirconium alloy used. Additionally, a coating deposition technology needs to be developed. The coating should not change its shape independently but change adaptively with the substrate. And finally, the coating should not affect the cladding properties.

All the above criteria can be potentially satisfied by elements forming the strongest oxide films. Zirconium oxide has an optimal formation temperature (and, consequently, strength) but undergoes phase transformations as temperature grows; aluminum and chromium oxides are less strong. Chromium oxide forms a relatively good barrier to oxygen diffusion, so almost every country started with chromium coatings.

Certain risks should be considered when using coatings. It is well known that any complexity added to a structure (for example, uniform part vs. coated part) increases the risk of failure. It is necessary to ensure proper adhesion of the coating in the process of zirconium's alpha to beta phase transformation and radiation-induced deformation. It is also necessary to maintain integrity of the coating when assembling fuel assemblies (pushing fuel rods through the spacer grid) and during operation (fretting corrosion). Besides, the diameter of fuel rods should remain unchanged so as to maintain the existing fuel assembly design. There is also a risk of failure (cracking) during operation, resulting in a more intensive corrosion process. There is no technology of depositing thick uniform coatings on 4-meter long fuel rod tubes, although there are different deposition techniques, such as vacuum-arc deposition, laser-induced vacuum arc deposition, magnetron sputtering, laser powder cladding in argon atmosphere, ultrasonic cold spray powder deposition, etc.

1.1.1. MAX-phase coatings

One of the coating option researchers are working on is the development of MAX-phase alloys [11]. MAX phases are a group of complex compounds (carbides and nitrides) where M is an early transition metal (for example, chromium, zirconium or titanium), A is an A-group element (mostly aluminum or silicon), and X is carbon or nitrogen. Their advantage is resistance to high-temperature oxidation at temperatures above 1,000°C, strong adhesion and coating strength, high thermal conductivity and stability, low coefficient of thermal expansion, and phase stability after weak neutron irradiation (up to 0.1 dpa). However, they also have critical disadvantages, such as low fracture toughness and ductility, noticeable interaction of aluminum and silicon with zirconium and other elements, and possibility of forming aluminum oxides in operating conditions (water soluble hydroxide – boehmite – forms in overheated water even at 300–350°C).

The specifics of depositing MAX-phase coatings on fuel claddings is that, in addition to the techniques specified above, other techniques can also be used, including hot isostatic pressing, self-propagating high-temperature synthesis, jet sintering, and spark plasma sintering of nitride and carbide powders.

Multi-layer coatings, for example Ti-N and Ti-Al-N, were obtained in a series of experimental studies [12]. They were tested for resistance to corrosion in water, steam and vacuum at a wide range of temperatures, as well as for compression, tension and adhesion. These coatings were also irradiated in research reactors and were found to behave not as desired because certain nitrides were observed to dissolve.

1.1.2. Steel coatings

An advanced alloy is an iron, chromium and aluminum (Fe-Cr-Al) alloy with different additives. Its advantages are good adhesion and density, notably slow oxidation dynamics, coefficient of thermal expansion close to that of zirconium, and no reaction with steam at a temperature of up to 1,300°C. This coating also strengthens the cladding. However, it is unlikely to be used in practice because of its numerous drawbacks that manifest themselves during operation. All the coating components dissolve in zirconium and form intermetallics, which means that a barrier layer between the coating and the cladding is required. In addition, chromium and aluminum absorb more neutrons than zirconium so that fuel enrichment is required. And the coating is brittle as well.

There are different deposition techniques for Fe-Cr-Al coatings. For example, Korean researchers [13] solved two tasks (cladding strengthening and corrosion resistance improvement) by depositing micrometric coating layers. They first applied powdered iridium oxide on the zirconium fuel rod and fused it with a laser beam; this layer was then covered by a Fe-Cr-Al or chromium finish coating. Yttrium oxide or molybdenum was used as a barrier layer.

Tests showed that a molybdenum interlayer between Fe-Cr-Al and zirconium virtually prevented the formation of zirconium oxide. In other words, Fe-Cr-Al and molybdenum slow down the diffusion so that oxygen does not get into zirconium. Tests were done on tubes: their internal surface oxidized to the depth of 100 μm, or 10 times deeper than during operation.

Multi-layer coatings are developed at the Massachusetts Institute of Technology: the cladding is first covered with a Cr-Mo layer, then a niobium interlayer, and finally with Fe-

Cr-Si and zirconium nitride [14]. The structure becomes very complex, with several oxides formed, including chromium oxide ($FeCr_2O_4$), silicon oxide (Fe_2SiO_4) and iron oxide.

The above deposition techniques are, in fact, components of different 3D coating technologies. But 3D is a casting technology, and cast products are prone to structural discontinuities (segregations at grain boundaries, non-uniform grains, etc.). There are just a few alloys obtained by unidirectional solidification of molten metals. It is therefore needed to develop a new technique for the production of tubes with this technology. This is where know-how and best practices in 3D printing can be useful. Obtaining the desired structure and phase in cast products is further complicated by such problems as finding optimal alloys and subsequent treatment of cast layers.

1.1.3. Fuel cladding alternatives

Fe-Cr-Al alloy is an alternative cladding material studied currently at the Oak Ridge National Laboratory [15]. As high-temperature oxidation begins, a chromium oxide (Cr_2O_3) film is formed and protects the material from oxygen diffusion. But when the temperature exceeds 1,000°C, the oxide turns into hydroxide and dissolves. Besides, chromium can vaporize, pass through the oxide layer and get into the coolant. Nonetheless, the process results in the formation of aluminum oxide that can withstand temperatures of up to 1,300–1,400°C. These claddings are currently undergoing tests in the USA.

One may ask whether it is possible to make steel claddings. As mentioned above, steel has an inherent disadvantage – it is prone to stress corrosion cracking. Much progress has been made, though, in the development of radiation-resistant steel (mostly austenitic and ferritic/martensitic steel grades) since the 1950s. New steel grades have a much better resistance to irradiation and cracking. Work is continuing to study the chemical composition

of such claddings. It will be necessary, though, to either increase the fuel enrichment or make the cladding walls very thin so that they capture as few neutrons as possible.

Another interesting alternative – molybdenum cladding – is offered by American researchers [16]. The best option so far has been developed by EPRI (Electric Power Research Institute) and GE (General Electric). It is a thin-wall molybdenum tube coated from two sides to prevent oxidation and subsequent oxide degradation, which starts at 700°C. Molybdenum tubes can be protected with zirconium as it forms a strong oxide, which is a good barrier against the oxygen and hydrogen diffusion in molybdenum. Additionally, it is possible to use complex alloys with corrosion-resistant steel, such as Fe-Cr-Al.

The possibility of using composite cladding materials, such as silicon carbide, is discussed widely. The cladding can have several layers – an external monolith SiC layer, an intermediary SiC fiber layer, a phase-boundary layer, and an internal monolith SiC layer [17]. Such tubes will be functional provided that the drawbacks inherent in SiC and SiC//SiC composites are overcome. First, it is necessary to maintain the composition stability of this carbide as any deviation will result in the presence of free silicon, which will react with uranium and form a eutectic mixture. Second, silicon carbide like other ceramic materials has very low ductility and fracture toughness. As a result, stresses caused by fuel swelling cannot be relaxed by plastic deformation and should be accounted for in the design of such fuel rods. Third, porosity is inevitable in composite materials produced by impregnation even if powder technology is used. And a porous cladding is nonsense because fuel emits fission products, and there is xenon and krypton under the cladding. If it is porous, there is no nuclear safety. Fourth, there is no sealing technique for such ceramic materials. Since

they cannot be welded, other methods should be found. Fifth, ceramic tubes often have an irregular (oval) section and their surface is not smooth due to the use of powder technology.

1.1.4. Chromium coatings

Advantages of chromium coatings include a high melting point, high corrosion resistance in overheated water (up to 1,000°C), and high thermal conductivity. However, they have a number of critical disadvantages. First, chromium is very brittle by nature. The element has a very low relative elongation, and it does not increase when the coating is applied. Second, chromium diffuses into zirconium's BCC lattice to a significant depth. Besides, chromium and zirconium form a brittle phase ($ZrCr_2$) and a eutectic mixture at the temperature of 1,332°C. Third, chromium has a larger neutron capture cross section than zirconium – chromium-coated claddings might thus need a higher enriched ^{235}U fuel.

Positive results were obtained when testing chromium coatings for resistance to oxidation in water and steam at a wide range of temperatures (350–1,200°C), as well as resistance to tear, creep, cladding swelling and welding. Irradiation tests began in research reactors. The best results in creating multi-layer chromium and niobium-chromium-titanium coatings were achieved by French researchers. They have developed a magnetron sputtering technique for the deposition of coatings on full-length fuel rods [18].

According to recent studies chromium-based coatings applied to zirconium alloys besides having high corrosion resistance during normal reactor operation and high oxidation resistance during lost coolant accidents, have other very useful properties:

– increased durability (5 times lower mass loss on the average) [19];

– increased resistance to corrosion in steam at 1,200°C (20 times lower mass gain over 2 hours) [20];

– decrease hydrogen permeability: it is shown in [21] that the amount of hydrogen absorbed by Zy-4 alloy with a 10 μm Cr coating after a 4-hour oxidation in steam at 1,000°C does not exceed 80 ppm; it is shown in [22] that the amount of hydrogen in chromium-coated zirconium (Zr) samples after the autoclave test (400°C, 200 atm) decreases from 5.5 to 0.1 molecules of H_2 per gram;

– ensured oxidation according to the parabolic law (no linear oxidation) [23].

As known, lower hydrogen permeability of the surface layer contributes to maintaining ductility of zirconium alloys. As shown in [21], application of a chromium-based coating extends the time (from 30 to 80 minutes) of cladding failure caused by embrittlement (impact toughness (KCU) decreasing to 3 J/cm^2) after oxidation in steam at 1,200°C and water quenching.

From the other side studies show that under the reactor's standard operating conditions (360°C and 5.5 PH of water solution), pure Chromium dissolves at 0.1 mg/cm^2 over 300 days of testing. Possible solution could be Chromium coating doped with aluminum (6–30%), which eliminates dissolution of zirconium in water under standard conditions by forming spinel $(Cr,Al)_2O_3$ on the surface [20]. Formation of Zr–(22 at.%)Cr eutectic mixture (Tm = 1,332°C) leads to a complete degradation of the coating's protective properties at a temperature above 1,330°C. In this situation, Zr diffusion to the external oxidation surface of the fuel rod cladding results in quick melting of the eutectic mixture and its diffusion into the sample. As shown in [24], the entire chromium layer diffused into the fuel rod cladding after a 2-minute oxidation in steam at 1,400°C. Formation of a eutectic mixture can be avoided by applying a layer of chromium nitride [24] or nitrides of Ta, Mo, Nb or W [21] or their certain isotopes that have a low thermal neutron capture cross section.

1.1.4. Previous work on chromium radiation resistance

Radiation resistance of any coating deposited on fuel cladding must be as high as zirconium alloy underlayer. Neutron and heavy ion irradiation data as well as void swelling behavior analysis on pure chromium in a form of bulk material or coatings is very limited and requires additional research efforts.

The radiation response of chromium has not been studied in the West, but this metal in both lightly and heavily alloyed forms was considered as a potential fast reactor cladding material in the Soviet Union. Several low-alloyed chromium candidates were irradiated with neutrons in Research Institute of Atomic Reactors in Russia and were also irradiated with Cr ions in the Kharkov Institute of Physics and Technology in Ukraine. The latter laboratory also irradiated pure chromium for comparison. Some data were published in Western journals but most of the data from these studies are available only in older, internal and limited-distribution reports written in Russian.

Three low alloying chromium-base alloys were irradiated in Russia, using both the SM-2 mixed spectrum reactor and the BOR-60 fast reactor to doses as high as 45 dpa, with one low alloying chromium alloy designated BH-3K with minor additions of La, V, Ta and C (<1% total) reaching swelling levels of 2.2 to 2.8% at 650-750°C and doses of 40-45 dpa. One significant surprise was that swelling was observed at all temperatures studied in the 400-829°C range. All temperatures well above the normal operation range of PWRs, temperatures lower than 400°C were not examined since these experiments were directed primarily toward fast reactor application. According to these studies the ion-induced swelling rate of pure chromium at 650°C appears to be on the order of ~0.03%/dpa, it also

appears that swelling at very low doses involves a higher swelling-rate transient since the data do not extrapolate back to zero swelling [25].

The data range quoted above was expanded and the data used in an open literature paper by Bryk et al. as a base for comparison of the ion-induced swelling of three chromium-base alloys, with the conclusion that the swelling behavior was not too sensitive to the minor low alloying composition, although the pure Cr data was not covered in any depth in this paper [26]. In Bryk's open literature paper the irradiations were conducted to doses as high as 180 dpa over the range 550-800°C. Swelling reached ~9% at 180 dpa and 730-750°C in one of the chromium-base alloys but was observed to develop significant spatial heterogeneity arising from phase decomposition of the alloys. It was noted that voids developed almost immediately at very low doses in both pure chromium and the alloys. One micrograph was presented that showed that one of the alloys exhibited development of void ordering into a superlattice, but the temperature at which ordering was not specified in the paper by Bryk.

Kuprin et al., also in Ukraine at the same laboratory, more recently studied swelling of pure arc evaporation deposited chromium induced by 1.4 MeV Ar ion irradiation at 400°C to 5, 15, and 25 dpa [27]. They found swelling of 0.16% at 5 dpa and 0.66% at 25 dpa, again suggesting a swelling rate of ~0.03%/dpa at 400°C. No mention was made of void ordering in this study. Kuprin's primary conclusion was that swelling in chromium appears to be too small to be a major concern in light water reactor applications where the dose of fuel cladding would never reach 25 dpa. This study suffers somewhat from the use of a rather shallow-penetrating ion, requiring data extraction very close to the surface (~100 nm) in order to avoid the very strong effect of the injected interstitial. If there is a strong effect of

temperature on the swelling it was not explored in this single temperature experiment, but the combined results of both the Bryk and Kuprin studies imply that while there is a temperature dependence of the void size and concentration distributions, the post-transient swelling rate is very small at ~0.03%/dpa and not very sensitive to irradiation temperature over the range of 400-700°C. Note that both the Bryk and Kuprin studies were conducted on the same accelerator (ESUV-1) but years apart and with different ions, different energies and different dpa rates.

Another published Russian report addressed the phase stability and void swelling at 600-750°C in BOR-60 of two highly alloyed candidates, Cr-10Fe-Zr,Y and Cr-35Fe-Zr,Y [28]. For the purposes of the current study it is sufficient to note that swelling was observed in these alloys under most irradiation conditions.

1.2. References

[1] International Atomic Energy Agency, Nuclear Power Reactors in the World, Reference Data Series No. 2, IAEA, Vienna (2017).

[2] Zirconium Alloys for LWR Fuel Cladding and Core Internals, Suresh Yagnik, Anand Garde, in Structural Alloys for Nuclear Energy Applications, 2019.

[3] K. Krenz, Deep Waters: The Ottawa River and Canada's Nuclear Adventure (McGill-Queen's University Press, 2004), p. 95.

[4] "Fact Sheet on the Three Mile Island Accident". US Nuclear Regulatory Commission. Retrieved December 18, 2008.

[5] Chernobyl - A Continuing Catastrophe, United Nations Office for the Coordination of Humanitarian Affairs (OCHA), 2000.

[6] IAEA Report by the Director General on The Fukushima Daiichi Accident, STI/PUB/1710 (ISBN:978-92-0-107015-9), September 2015.

[7] World Nuclear Association, Fukushima Daiichi Accident, Updated October 2018.

[8] Nuclear Applications: Zirconium Alloys, S. Banerjee, M.K. Banerjee, in Reference Module in Materials Science and Materials Engineering, 2016.

[9] Nuclear Power Development in the USSR, IAEA publication, A.M. Petrosyants, Chairman of the USSR State Committee on the Utilization of Atomic Energy, Speech delivered at the Atomic Industrial Forum in Washington, 1989.

[10] Investigation of Stainless Steel Clad Fuel Rod Failures and fuel performance in the Connecticut Yankee Reactor, EPRI NP-2119, Project 1758-1, Final Report, November 1981.

[11] Garcia-Diaz, Brenda & Olson, Luke & Verst, C. & Sindelar, Robert & Hoffman, E. & Hauch, Benjamin & Maier, Benjamin & Sridharan, K. (2014). MAX phase coatings for accident tolerant nuclear fuel. Transactions of the American Nuclear Society, 110, p. 994-996.

[12] Multilayer (TiN, TiAlN) ceramic coatings for nuclear fuel cladding, Ece Alat, at al, Journal of Nuclear Materials 478 (2016), p. 236-240.

[13] Park, Dong Jun & Kim, Hyun-Gil & Jung, Yang & Park, Jung Hwan & Yang, Jae Ho & Koo, Yang-Hyun, Behavior of an improved Zr fuel cladding with oxidation resistant coating under loss-of-coolant accident conditions, Journal of Nuclear Materials 482 (2016).

[14] Mechanical analysis of surface-coated zircaloy cladding, Youho Lee, Jeon Ik Lee, Hee Cheon NO, Nuclear Engineering and Technology, Volume 49, Issue 5, August 2017, pp. 1031-1043.

[15] Thermo-mechanical analysis of SiC and FeCrAl cladding behavior under a loss-of-coolant accident, Prepared for U.S. Department of Energy, 2018.

[16] Molybdenum alloys for accident tolerant fuel cladding. High temperature corrosion and oxidation behavior, Kim, Young-Jin (GE Global Research Center, Schenectady, NY (United States)); Cheng, Bo (Electric Power Research Institute, Palo Alto, CA (United States)); Chou, Peter (Electric Power Research Institute, Palo Alto, CA (United States)), Proceedings of 2014 water reactor fuel performance meeting/ top fuel / LWR fuel performance meeting (WRFPM 2014).

[17] SiC/SiC Cladding Materials Properties Handbook, T. Koyanagi, Y. Katoh, G. Singh, M. Snead, ORNL/TM-2017/385, 2017.

[18] On-Going Studies at CEA on Chromium Coated Zirconium Based Nuclear Fuel Claddings for Enhanced Accident Tolerant LWRS Fuel, Brachet, Jean-Christophe at al., TopFuel 2015, (13-19 Sept. 2015), Zurich, Switzerland.

[19] Bischoff J., Delafoy C., Vauglin C. et al. AREVA NP's enhanced accident-tolerant fuel developments: Focus on Cr-coated M5 cladding. In: Nuclear Engineering and Technology, 2018, vol. 50, pp. 223–228.

[20] Kim H.-G., Kim I.-H., Jung Y.-I. et al. Chromium-aluminum binary alloy having excellent corrosion resistance and method of manufacturing thereof. In: KR Patent 101691916 B1. № 20140141522A; fi l. 20.10.2014; publ. 27.12.2016. P. 15

[21] Brachet J.-C., Billard A., Schuster F. et al. Nuclear fuel cladding, manufacturing processes and use against oxidation. In: FR patent 3025929 A1. № 1458933; fi l. 17.09.2014; publ. 21.10.2016. P. 43.

[22] Ivanova S.V., Glagovskii E.M., Khazov I.A. et al. [Modification of the surface of zirconium components of fuel assemblies of thermal-neutron reactors in order to increase their operational properties]. In: Fizika i khimiya obrabotki materialov [Physics and Chemistry of Materials Treatment], 2009, no. 3, pp. 5–17.

[23] Kuprin A.S., Belous V.A., Bryk V.V. et al. [Vacuum-Arc Chromium Coatings for Zr-1Nb Alloy Protection Against High-Temperature Oxidation in Air]. In: Voprosy atomnoi nauki i tekhniki [Problems of Atomic Science and Technology], 2015, no. 2 (96), pp. 111–118.

[24] Daub K., Persaud S.Y., Rebak R.B. et al. Investigating Potential Accident Tolerant Fuel Cladding Materials and Coatings. In: Proceedings of the 18th International Conference on Environmental Degradation of Materials in Nuclear Power Systems – Water

Reactors. 13-17 August 2017, Portland. Vol. 2. Springer International Publishing, 2018. pp. 215–234.

[25] V.Bryk, V.N.Voevodin, V.F.Zelenskiy, B.V.Matveenko, I.M.Nekhludov, V.K.Horenko, T.P.Chernyaeva, A.N.Rakitskiy, V.I.Trefilov, Investigation of radiation swelling of the deformed minor-alloyed Cr alloy under its irradiation at the accelerator. VANT 1981, pp. 33-38 (in Russian).

[26] V.V. Bryk, V.N. Voyevodin, I.M. Neklyudov, A.N. Rakitskij, Microstructure investigation of Cr and Cr alloys irradiated with heavy ions, Journal of Nuclear Materials 225 (1995) 146-153. Nuclear Materials 225 (1995) pp. 146-153.

[27] A.S. Kuprin, V.A. Belous, V.N. Voyevodin, R.L. Vasilenko, V.D. Ovcharenko, G.D. Tolstolutskaya, I.E. Kopanets, I.V. Kolodiy, Journal of Nuclear Materials 510 (2018), pp. 163-167.

[28] V. Chakin, V. Kazakov, Yu. Goncharenko, Z. Ostrovsky, "Formation of the σ-phase in Cr-Fe alloys under irradiation", Journal of Nuclear Materials 233-237 (1996), pp. 573-576.

[29] Terrani, Kurt A. Accident tolerant fuel cladding development: Promise, status, and challenges. United States: N. p., 2018.

[30] The State of the Art Report on the Development of Advanced Nuclear Fuel Cladding Tube KAERI/AR-597/2001.

[31] S.J. Zinkle, K.A. Terrani, J.C. Gehin, L.J. Ott, L.L. Snead, Accident tolerant fuels for LWRs: A perspective, J. Nucl. Mater. 448 (2014) pp. 374–379.

[32] L.J. Ott, K.R. Robb, D. Wang, Preliminary assessment of accident-tolerant fuels on LWR performance during normal operation and under DB and BDB accident conditions, J. Nucl. Mater. 448 (2014) pp. 520–533.

2. EXPERIMENT PROCEDURE: EQUIPMENT AND TECHNIQUES

2.1. Samples preparation

The chromium was obtained from American Elements Inc. with purity >99%. Sample came in a shape of a coupon (Figure 2.1), with dimensions of 25 mm × 25 mm × 4 mm, it was originally cut using a low speed saw with IsoCut^{TM} Fluid (oil base coolant).

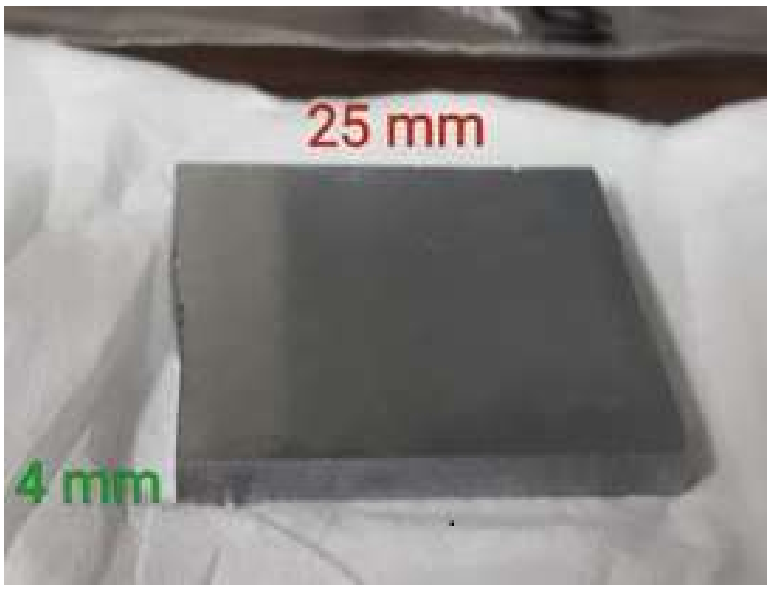

Figure 2.1 Pure chromium coupon as received.

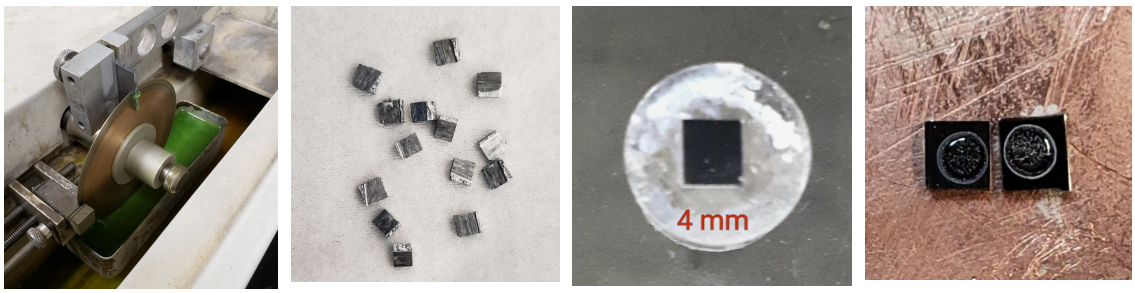

a) b) c) d)

Figure 2.2 Steps of specimen preparation: a) cutting a coupon with Isomet 1000, b) unpolished samples, c) mechanically polished samples, d) electropolished samples.

2.1.1. Cutting

Using IsoMet 1000 precision cutter (Manufactured by Buehler) in TAMU Microscopy Imaging Center the coupon was cut to smaller samples with dimensions of 4 × mm × 4 mm × 1.5 mm (Figure 2.2, a, b). The IsoMet 1000 was used because it helps to cut samples with minimum deformation, as this machine uses only gravity fed force. Also it has an ability to hold samples of all forms and shapes and is extremely helpful in cutting such as brittle material as chromium. For a smoother cutting a silicon carbide (SiC) cut-off blade 80-11195 (Allied) was used.

2.1.2. Manual polishing

Cut samples were first manually polished down to about 1 mm thickness using Nano 2000 polisher (Manufactured by Pace Technologies) with a rough SiC paper (320 grit), and later with grits 600 (26 μm), 1200 (15 μm), 800 (P-2400, 10 μm), and finally 1200 (P-4000, 5 μm) (Figure 2.2, c). The thickness of only 1mm was chosen to minimize any temperature gradient between the specimen surface and the target hot stage, producing <2°C temperature rise based on a finite element analysis considering both black body radiation and beam power deposition. After mechanical polishing specimens were sonicated in acetone for 5 minutes with Ultrasonic cleaner 1510 (Manufactured by Branson) to clean them from any remaining residues. As a final step, specimens were cleaned with methanol and dried with N_2 gas.

2.1.3. Electropolishing

Each of the specimens was polished further with a Tenupol 5 twin jet electro-polisher. The polishing solution used was 5% perchloric acid in methanol. The solution temperature was cooled to be ~20°C with an external liquid nitrogen bath. Each specimen was mounted in the sample holder and placed in the polishing unit. The polishing time was

~20 seconds per sample with a voltage bias of 20 V. After polishing, samples were repeatedly rinsed in methanol. Final sample produce can be seen on Figure 2.2, d.

2.1.4. Surface Examination

Before irradiation it is important to make sure that samples surface quality is met. Lyra 3 FIB-SEM (Manufactured by Tescan) at MCF was used to check the surface quality. Figure 2.3 shows an SEM image of chromium sample surface taken by Lyra 3 FIB-SEM with 10 kV operation voltage, clear difference can be seen between mechanically (no grains, scratches) and electropolished areas (clear grains, smooth surface). Figure 2.4 shows a close-up image of electropolished area. Grain boundaries are visible, with no deep scratches within the grains, both indicating that there was no significant residual surface deformation. The typical grain size was found to be ~100 μm.

After checking surface with SEM specimens are removed from the holders, bottom side is cleaned with acetone to remove copper tape residue and later top surface is cleaned with methanol before irradiation and quickly after dried with nitrogen gas blower gun, to remove residual methanol from the sample surface. For high temperature irradiation of pure chromium, it was important to clean specimens properly to prevent surface contamination during irradiation.

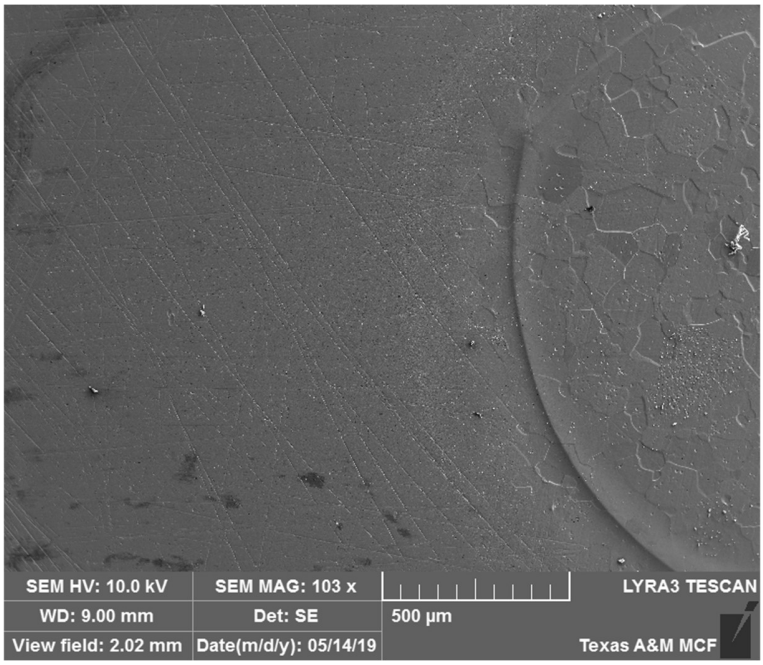

Figure 2.3 SEM SE image of mechanically and electropolished pure Cr surface.

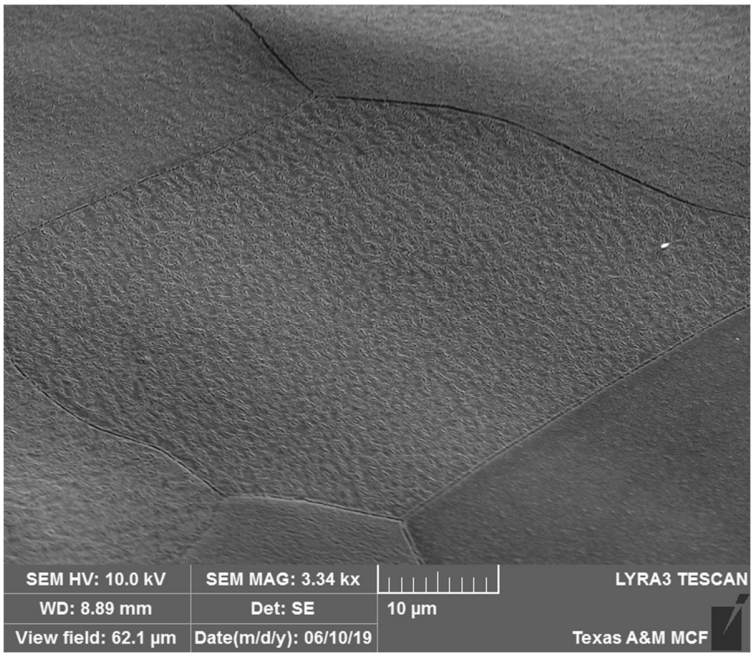

Figure 2.4 High magnification SEM SE image of electropolished pure Cr surface.

2.2. Irradiation Using Pelletron Accelerator

The National Electrostatic Corp. 3 MV Pelletron Accelerator was used for chromium samples irradiation. Pelletron Accelerator [1] is operated based on a simple principle. A beam of negative ions is injected into the accelerator from low energy end; once the beam reaches the HV terminal, the negative ions lose the extra electron plus one or more electrons in the stripping canal rich in nitrogen and positive ions are generated; these ions are accelerated one more time through the second tube at high energy end and exit the accelerator.

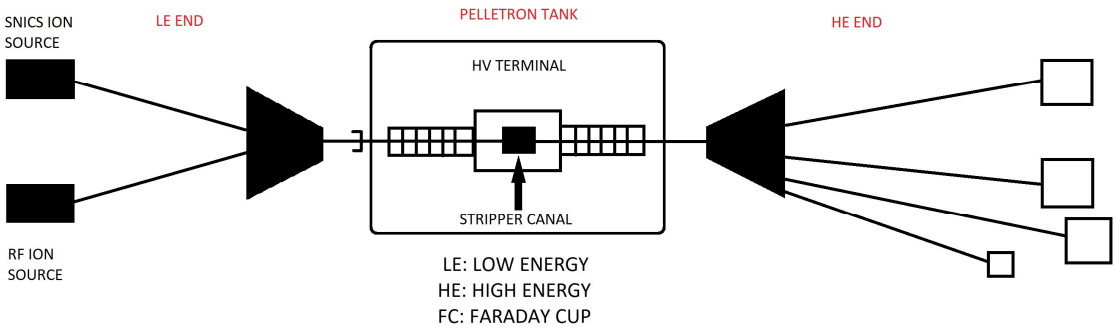

Figure 2.5 TAMU 3 MV Tandem Accelerator layout.

Full NEC 3 MV accelerator system structure:

1) Injection beamlines – consist of two ion sources (SNICS and RF), optical and diagnostic equipment;

2) Pelletron – consists of the pressure vessel, accelerator beamline, charging system;

3) High energy beamlines – consist of optical and diagnostic equipment starting from the exit of the Pelletron tank and include the work end stations and detectors in the end;

4) Control system – consist of hardware and software for accelerator system computer control.

2.2.1. Ion Sources and Injection Beamline

Injectors begin with two ion sources - RF Charge Exchange Ion Source or Alphatross (Figure 2.8) used for the production of He^- beams but can also produce H^-, NH^-, and O^- beams and Source of Negative Ions by Cesium Sputtering (SNICS) pictured on Figure 2.7. A heavy-ion SNICS source capable of creating negative ion beams from all elements that form a stable negative ion. The sources are followed by a bending magnet that focus the ion beam into the accelerator. Diagnostic equipment and other focusing elements are also an integral part of the injector.

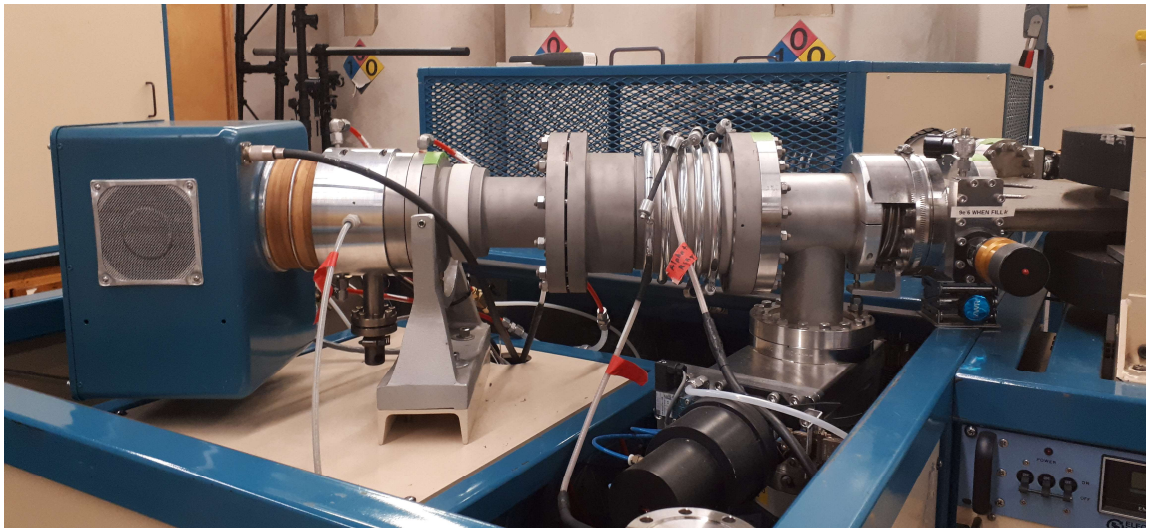

Figure 2.6 RF source without safety cage on a 3MV Pelletron accelerator system.

2.2.2. Source of Negative Ions by Cesium Sputtering (SNICS)

Principle of work of SNICS is following - accelerated cesium ions striking a cold cathode to produce a negative ion beam of cathode material.

Cesium vapor goes from the cesium oven into the area between the cathode, that is cooled and the hot ionizing surface (Figure 2.7). Majority or cesium becomes ionized by the heated surface, while little Cs amount condenses on the front of the cathode. Particles are sputtered from the cathode by the ionized cesium through a thin cesium layer on the cathode surface. As a result, negative ions are leaving the cathode surface and then accelerated toward the ionizer.

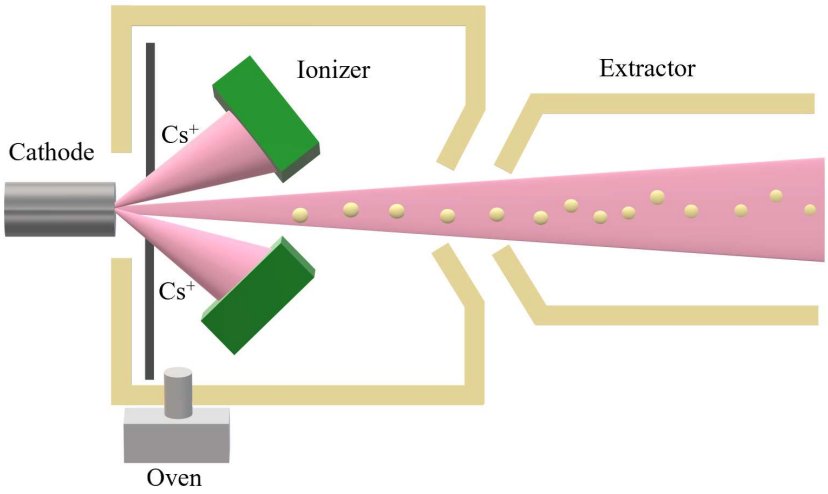

Figure 2.7 A diagram of the cesium sputtering operation produced by the SNICS.

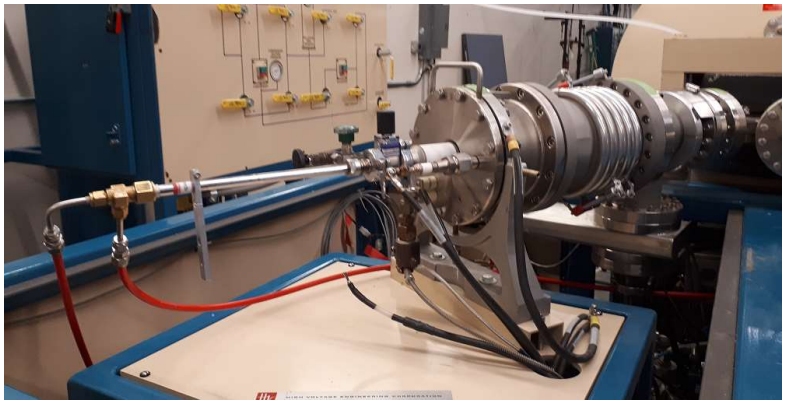

Figure 2.8 SNICS injector without safety cage on a 3MV Pelletron accelerator system.

2.2.3. Pelletron

Basic work principle of any electrostatic accelerator is that positive terminal attracts negative ion beams and accelerates positive ions away. Therefore, Tandem Pelletrons start with negative ions produced by SNICS.

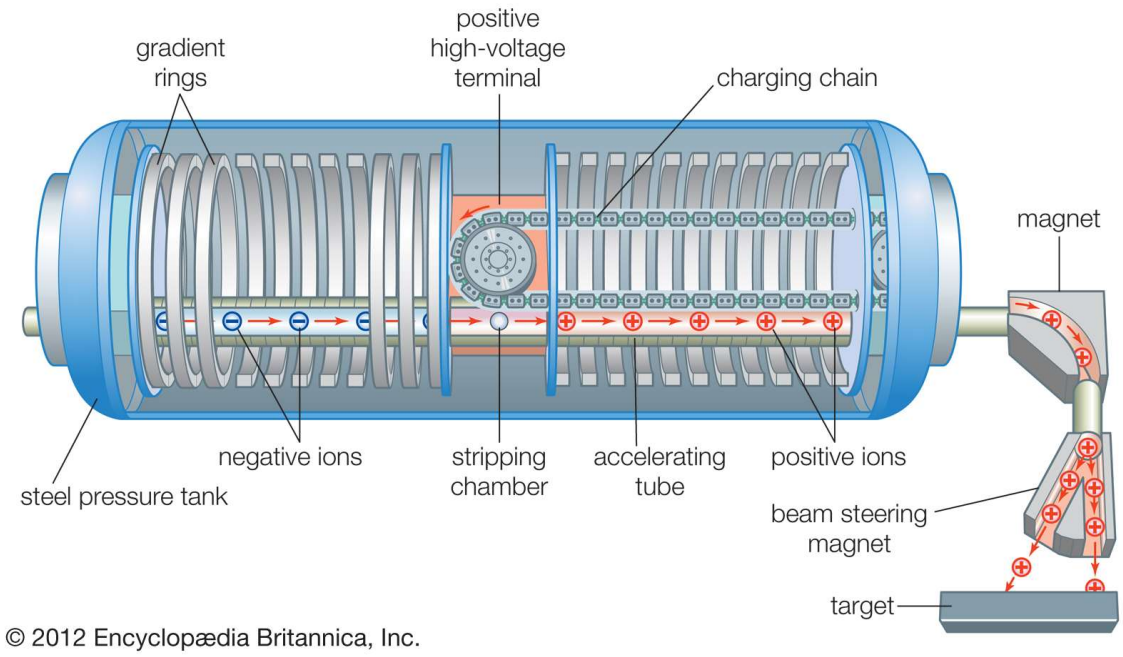

Figure 2.9 Tandem Pelletron Diagram.

Both ends of the Pelletron in tandem accelerator are at ground, high-voltage terminal is located the in the middle of the tank. Positively charged Tandem allows the negatively charged injected ions to accelerate to the terminal. A stripper inside the terminal which uses a nitrogen gas removes electrons from the incoming negative ions. Once positively-charged, ions receive a second boost of acceleration (hence the name “tandem”, ions go through double acceleration inside the Pelletron) exiting the terminal and travel acceleration tubes to the ground at the HE end of the tank.

Pelletron main parts:

- **Pressure vessel:** also known as Pelletron or tank, contains inside all the main parts - charging system, acceleration tubes, column/support structure, and gas stripper. The tank itself is divided into two sections: a bell section and an endplate (Figure 2.10).

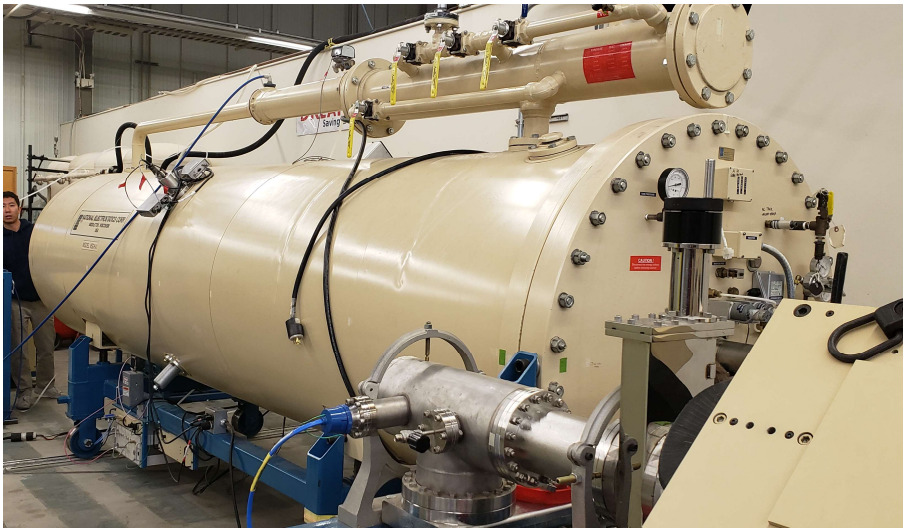

Figure 2.10 NEC Tandem Pelletron.

- **Charging system:** is the heart of NEC's accelerator technology. Figure 2.9 shows chain charging system. First negative inductor electrode, which is connected to external power supply, induces positive charge in pellets departing drive pulley for terminal end. Next pellets transfer positive charge to terminal via charging column, so called "up-charging". The third step allows negative suppressor electrode, that is connected to pickoff pulley, to prevent sparking as positively charged pellets make contact with terminal pulley. Positive inductor electrode connected to pickoff pulley induces negative charge in pellets departing terminal pulley for drive end. Pellets transfer negative charge from terminal via charging column, that is called "down-charging". Finally, positive suppressor electrode

(connected to external power supply) prevents sparking as negatively charged pellets make contact with drive pulley.

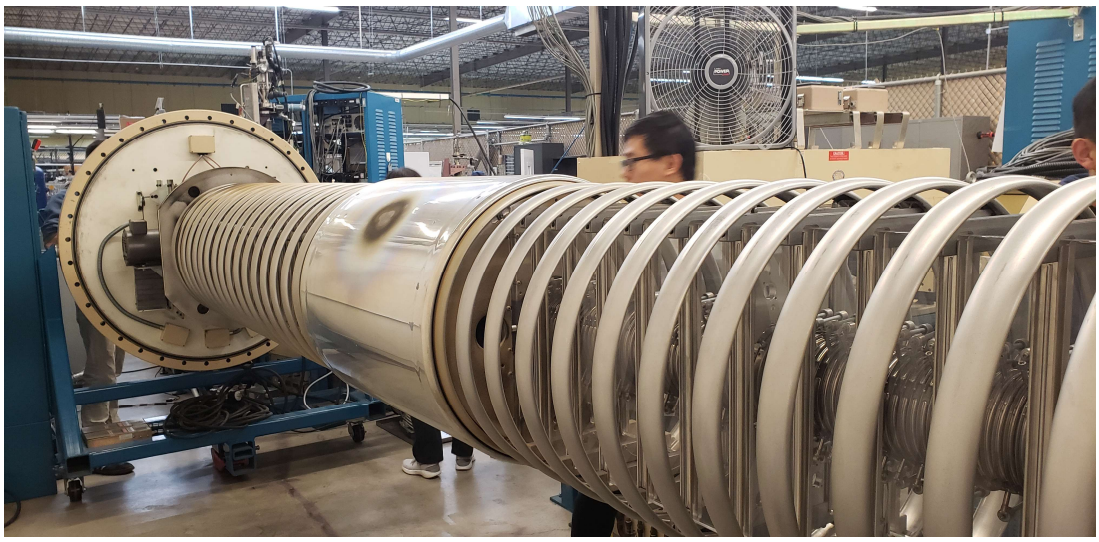

Figure 2.11 The column, connected to the endplate (left), is pulled out from the bell section of the tank for servicing.

- **Acceleration tubes:** are designed for operation in high pressure SF_6 gas. Metal and ceramic tubes are bonded into an assembly. No organic compounds are present in the vacuum volume. Tubes are fully bakeable to be used in contaminant free and ultra high vacuum operation.
- **Column or support structure:** is shown on a Figure 2.11 and consists of parallel Lucite plates (also called Plexiglas) surrounded by equipotential rings. Lucite plates are used also to support the acceleration tube. Terminal in the middle and large bulkheads on both sides support those plates.
- **Gas Stripper:** in gas stripper, nitrogen gas is delivered to the terminal through a supply bottle, amount of the gas coming in can be regulated outside the

tank. Turbo-molecular pump is used in the terminal to recirculate nitrogen flow to insure that only a very small amount of gas is coming to the acceleration tubes. To prevent contamination of the gas output of turbo-pump is equipped with a trap.

2.2.4. High Energy Beamline

Once the positive beam has been accelerated, it exits the tank and enters the focusing HE beamline, which continues to focus the beam. Switching magnet with several ports sends the beam to one of the multiple extended beamlines, which also has additional beam focusing, steering, and diagnostic.

Figure 2.12 Post acceleration switching magnet with extended beamlines.

2.2.5. Control System

The accelerator is operated by a centralized control system. The control console shown on Figure 2.13 is used for input and adjustment of all accelerator parameters needed

for the operation. The control console has a computer system, meters and knobs that assign and save beam parameters, and an oscilloscope is used to display signals.

Figure 2.13 Accelerator control console.

The computer system is configured with NEC accelerator control software, AccelNET (Figure 2.14). AccelNET operates the display and control functions using special database management system which operates in Linux multitask environment.

Accelerator parameters are displayed on a computer screen in two formats as seen on Figure 2.15: text pages with lists of parameters (two windows on the bottom) and diagram displays of the accelerator system layout (top page window). Control panel helps to adjust parameters by menu-driven restoration, it has increment/decrement buttons, and computer

keyboard can be used for desired parameter values input or assigning needed parameter to a specific knob for analog adjustments.

Figure 2.14 AccelNET computer system for accelerator operation.

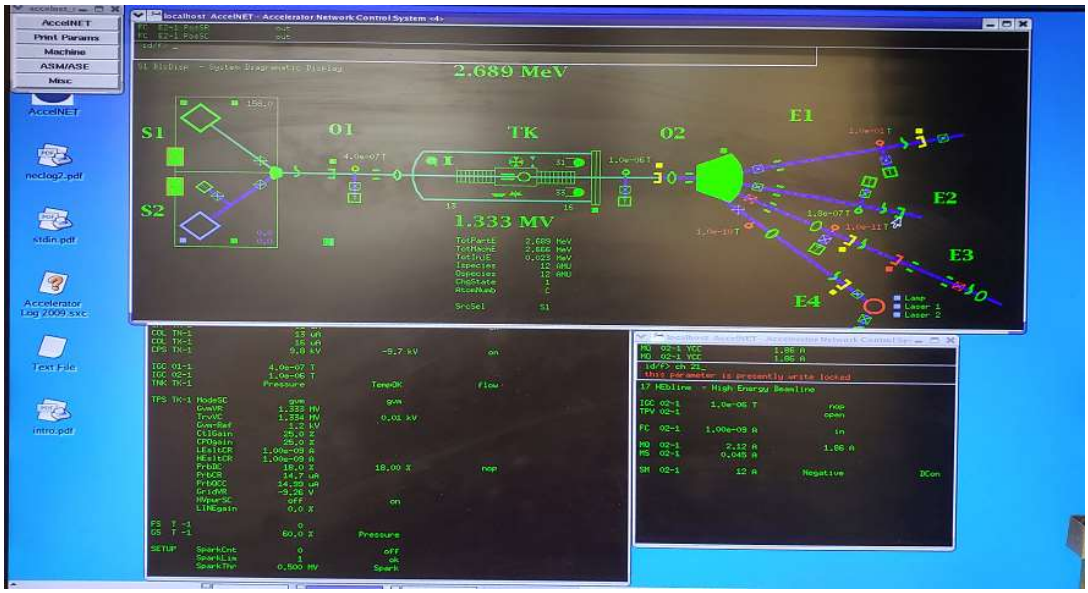

Figure 2.15 AccelNET screen layout.

2.2.6. Irradiation process

The 3 MV Tandem accelerator described in the sections above was used for pure chromium studies.

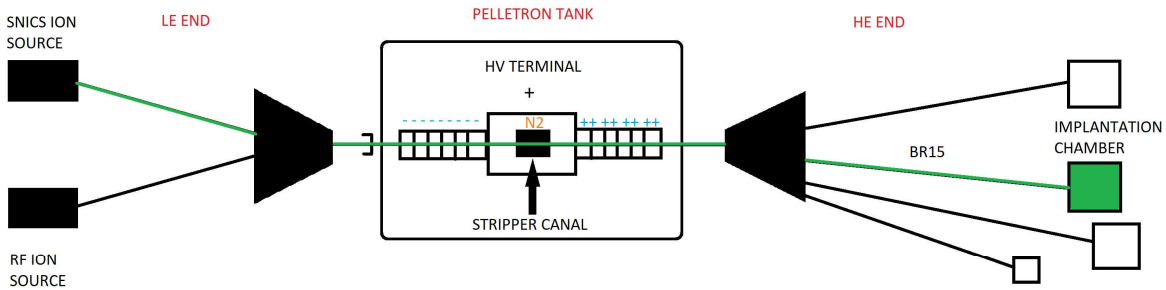

Figure 2.16 Fe^{2+} ion beam implantation scheme.

For this research pure Fe cathode solid bar was used in SNICS source in order to obtain 5 MeV Fe^{2+} ions. In SNICS source Fe ions leave the cathode surface and are accelerated toward ionizer by target voltage, and then further extracted by extraction voltage applied to extraction cone. From SNICS ion source Fe ion beam is fed to low energy magnet that is located between SNICS and Pelletron acceleration tank. The low energy magnet bends ion beam by applying magnetic field which makes it possible to select certain mass, Y-steerer helps beam positioning in vertical direction and Einzel lens focuses the beam before it is sent main acceleration tank.

When Fe negative ions enter the tank, they are accelerated toward positive high voltage terminal at the middle of the tank, and the electrons are stripped by injected nitrogen gas. Then, Fe negative ions become positive ions, and by losing electrons, they are charged needed 2+. After becoming positive, Fe^{2+} ions are repulsed away from the positive HV terminal.

.

Figure 2.17 Accelerator Low Energy End Equipment.

Once accelerated and focused by quadrupoles, Fe ion beam reaches the high energy magnet. Fe beam is selected by the magnet and directed to the specific beam line. For Fe implantation beam line R15 was used, which is located at 15° to the right.

After final beam adjustment (getting needed current, defocusing, deflection, setting beam size and shape), Faraday Cup at BR15 is open for a short time, about 5-10 sec, and beam is send to implantation chamber to burn a beam spot on white piece of paper taped on a copper target. Beam spot is checked for correct shape and uniformity.

For correct beam size and uniformity (Figure 2.18 a), the beam area is marked by marker on the copper stage and paper and copper tape are removed. To prevent any contamination during irradiation, the stage is cleaned with acetone to remove any adhesives from copper tape and cleaned once again with methanol. Then, samples are mounted by using water-based carbon free silver paste, and a heat gun is used to dry silver paste for better

adhesion (Figure 2.18 b). As a final step marker marks are removed with methanol. (Figure 2.18 c).

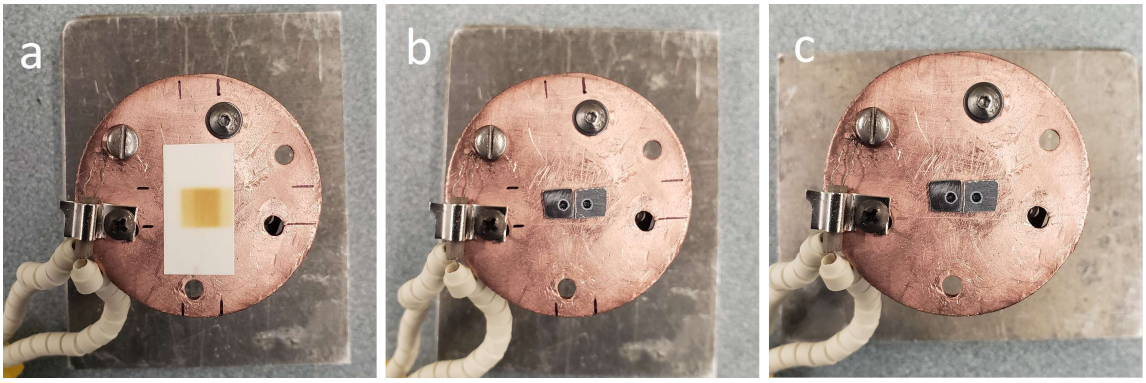

Figure 2.18 Process of Cr samples mounting on a hot stage.

All irradiations were performed using a static defocused beam to avoid void nucleation suppression characteristic of rastered beams [2]. The target chamber pressure during the irradiation was 6×10^{-8} torr or better. Prior to irradiation, the target chamber was baked at 200°C overnight. During irradiation, multiple beam deflectors were used to filter out contaminants such as C, N and O [3,4]. For this purpose three bending magnets located in BR15 beam line were used to deflect the beam in a zigzag way, so the contaminants with lower mass will be bent with higher angle and filtered out during this process. Liquid nitrogen trapping in the target chamber was applied to further improve the vacuum. A thermocouple attached to the hot stage was used for automatic temperature control. The temperature fluctuation during the irradiation was <5°C.

The total irradiation time T [s] was calculated using following equation:

$$T = \frac{F \times e \times q \times A}{I} \quad \text{Eq. 2.1}$$

Where,

F – fluence $\left[\frac{1}{\mathrm{cm}^2}\right]$,

e – elementary charge $1.602 \times 10^{-19}[\mathrm{C}]$,

q – ion charge state,

A – beam area $[\mathrm{cm}^2]$,

I – beam current $[\mathrm{A}]$.

The beam current was recorded every hour to adjust the total irradiation time. Hot stage temperature and vacuum condition are also closely monitored during experiments to avoid any unexpected fluctuations.

2.3. Sample Characterization

2.3.1. Scanning Electron Microscopy (SEM)

SEM images were obtained with the help of Tescan FERA-3 Model GMH FIB Microscope at Texas A&M Materials Characterization Facility (MCF), microscope is shown on Figure 2.19.

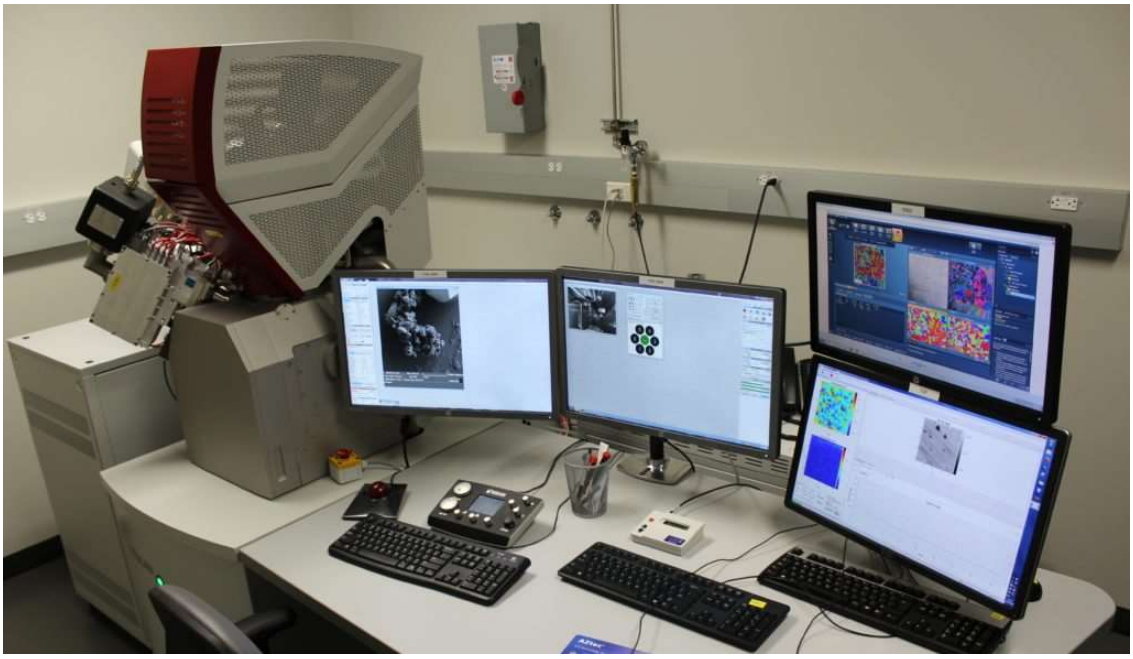

Figure 2.19 Tescan FERA-3 Model GMH Focused Ion Beam Microscope at Texas A&M MCF.

A Scanning Electron Microscope (SEM) uses focused beams of electrons to produce high resolution, 3D images. These images provide information on specimen topography, morphology and composition.

Figure 2.20 shows a working scheme of a typical SEM. At the very top of the microscope's column electrons are generated by the electron gun, which is a heated V-shaped tungsten filament. Electrons are then accelerated down the column. To prevent any molecules or atoms that may be present in the column from interacting with the electron beam, column should be under vacuum. Vacuum helps to ensure good quality imaging.

Electromagnetic lenses (located below the anode) are used to direct the path of the electrons. The condenser lens is responsible for the size of the electron beam (which defines

the resolution), while main role of the objective lens is to focus the beam onto the sample. Scanning coils raster the beam onto the sample.

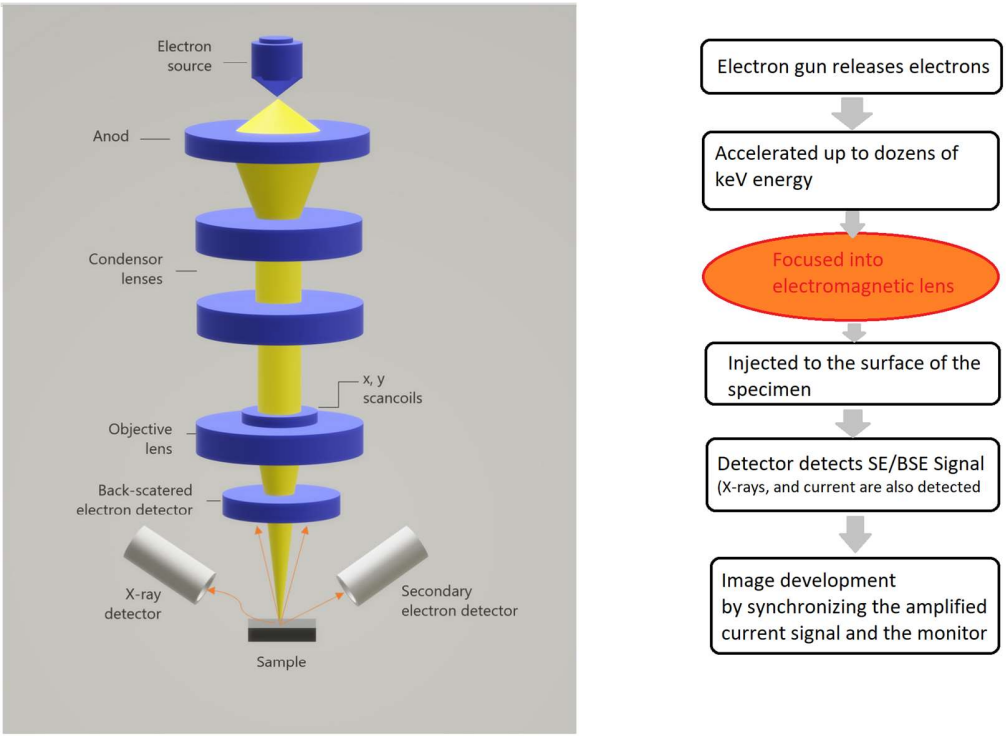

Figure 2.20 Schematic representation of an SEM system.

After interacting with the electron beam different types of electrons are emitted from samples. A Back Scattered Electron (BSE) detector is located above the sample and is used to detect backscattered electrons. One of the BSE use it to produce images that show contrast information between areas with different chemical compositions. For example, between Pt and Cr during FIB lift-out, Pt as a heavier element (it has high atomic number) will appear much brighter. A Secondary Electron (SE) detector is placed at the side of the electron

chamber. It is placed at an angle, that helps to increase the efficiency of detecting SE which helps to provide more detailed information about surface of the sample.

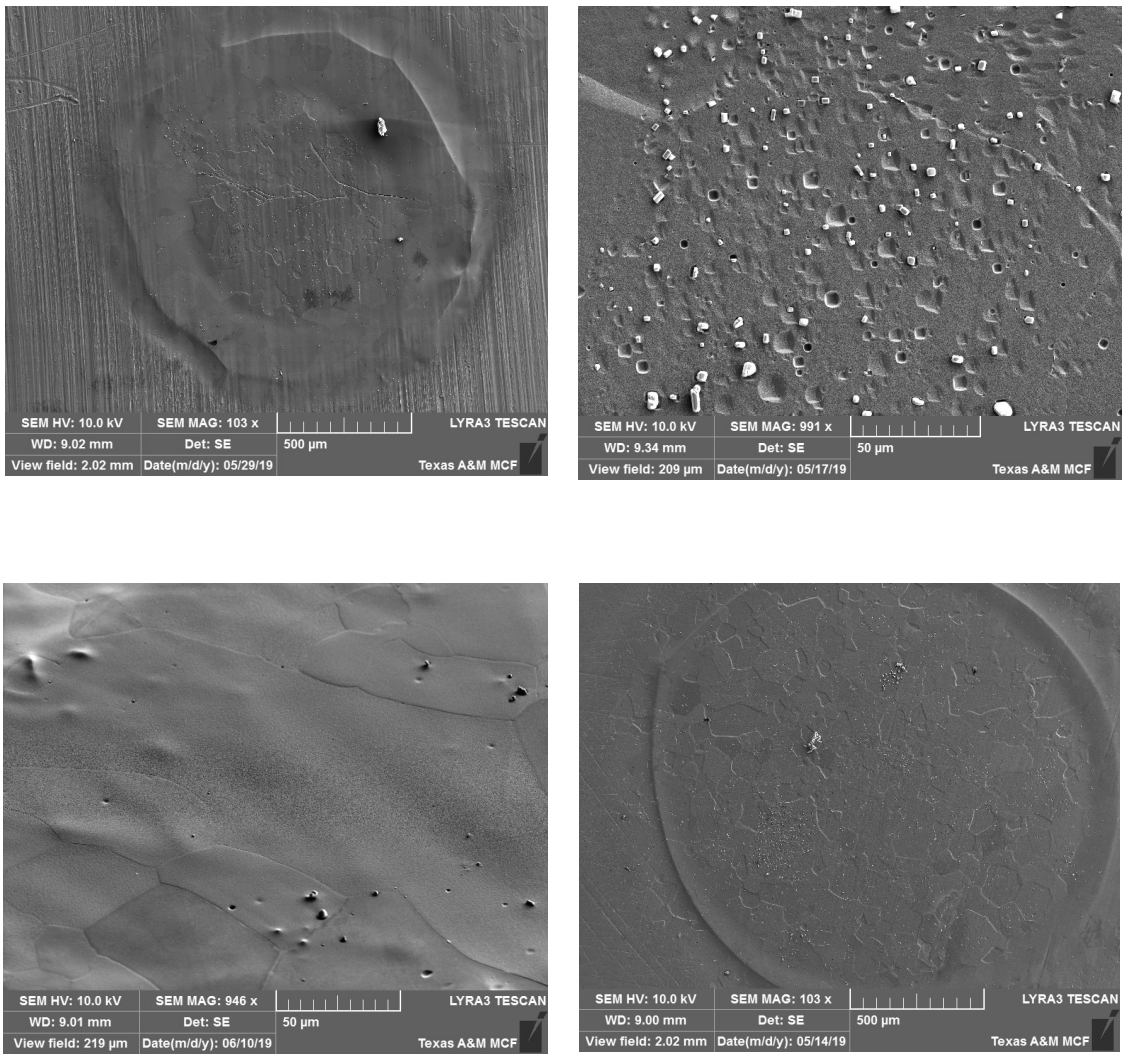

Figure 2.21 Typical SEM images of samples surface.

2.3.2. Transmission Electron Microscopy (TEM) Analysis

In this study, two Transmission electron microscopes were used: FEI Tecnai G2 F20 ST FE-TEM Materials - for bright field imaging and STEM and F20 FE-TEM – for measuring EELS thickness (Figure 2.22).

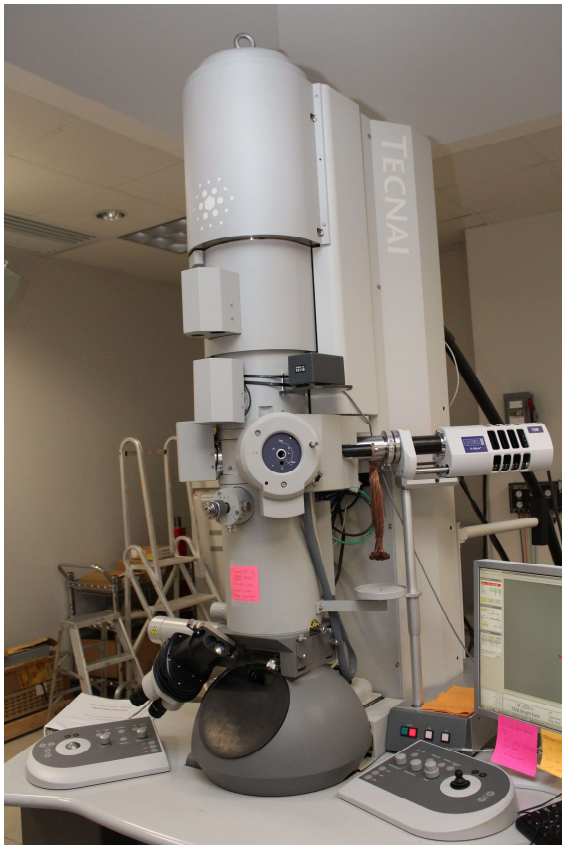

FEI TECNAI G2 F20 ST
FE-TEM – MATERIALS

FEI TECNAI G2 F20
FE-TEM

Figure 2.22 Transmission electron microscopes at Texas A&M MIC.

Transmission electron microscope (TEM) has four main systems shown on Figure 2.23:

(1) and (2) an electron gun, which produces the electron beam, and the condenser system, which focuses the beam onto the object,

(3) the image-producing system, consisting of the objective lens, movable specimen stage, and intermediate and projector lenses, which focus the electrons passing through the specimen to form a real, highly magnified image, and

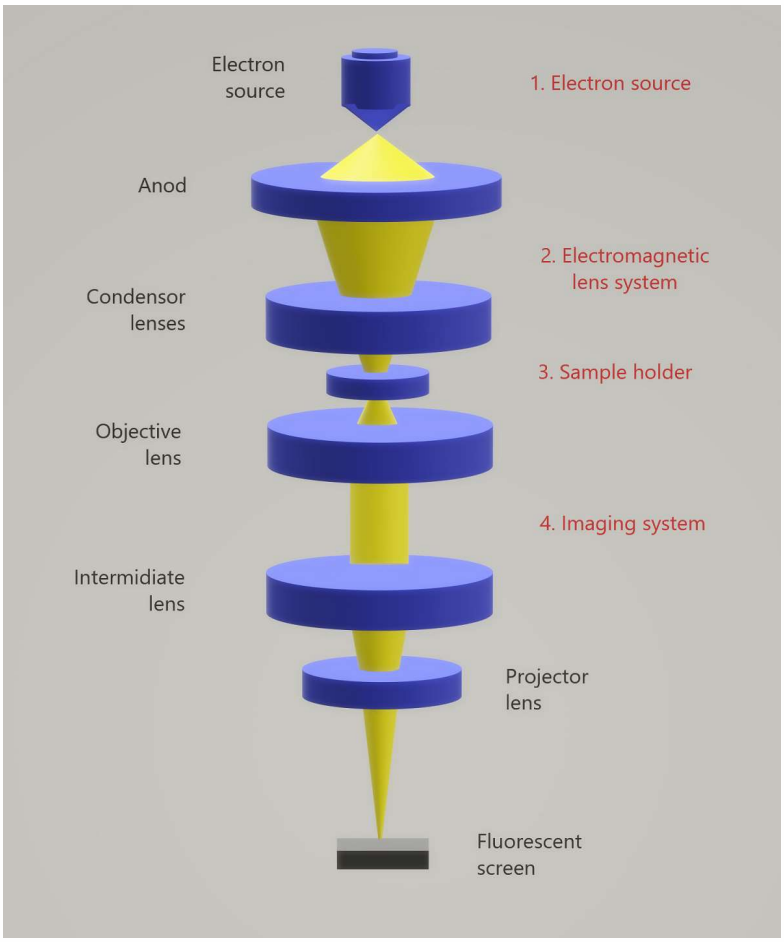

Figure 2.23 TEM main parts diagram.

(4) the image-recording system, which converts the electron image into some form perceptible to the human eye. The image-recording system consists of a fluorescent screen for viewing and focusing the image and a digital camera for permanent records. In addition, a vacuum system, consisting of pumps and their associated gauges and valves, and power supplies are required.

The condenser lens focuses the beam of electrons coming from the electron gun into a small, thin, coherent beam. The condenser aperture restricts the beam by excluding high angle electrons. The beam then reaches the sample and some part of it is transmitted, the amount of electron going through depends upon the sample thickness and its electron transparency. The objective lens focuses this transmitted beam portion into an image on a phosphor screen and charge coupled device (CCD) camera. Additional objective apertures are often used to enhance the contrast, these apertures block out high-angle unscattered electrons . To enlarge the image all the way it is passed down the column, where intermediate and projector lenses are placed.

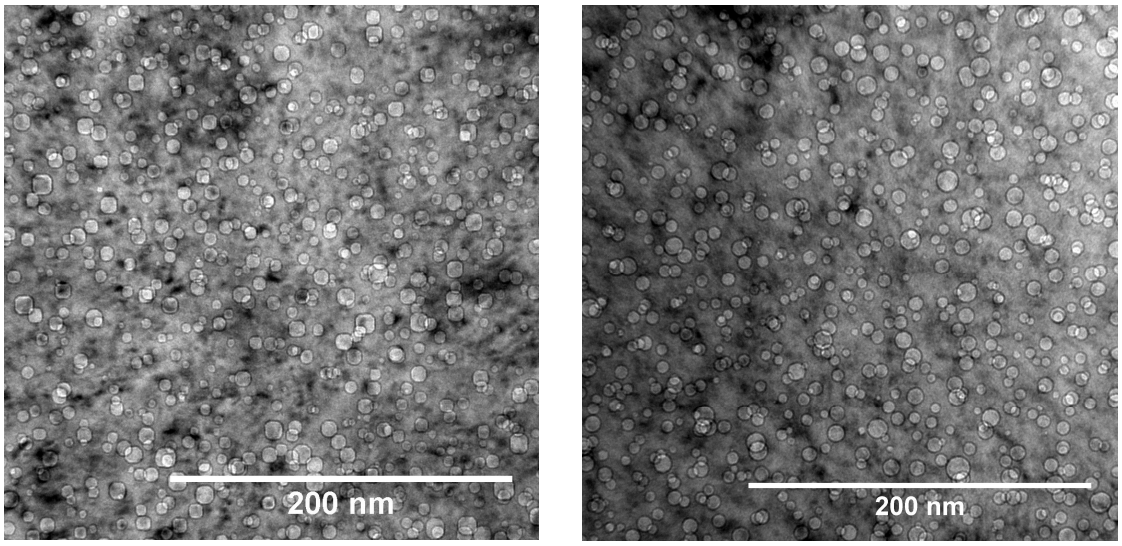

Figure 2.24 Typical bright field TEM images of Cr void swelling.

When produced and enlarged image strikes the phosphor screen, it generates the light, that allows the TEM user to see the image. Those areas of the sample that transmitted fewer electrons will appear darker on the image, while the areas that transmitted more electrons through look much brighter. In a way the bright field image works as a shadow of the specimen (Figure 2.17).

2.3.3. Scanning Transmission Electron Microscopy (STEM)

Scanning transmission electron microscopy (STEM) combines the principles of TEM and SEM.

Like TEM, STEM has requirements for the specimen thickness (very thin lamellae needed) and looks primarily at electrons that were transmitted by the sample. One of its principal advantages over TEM is that STEM can also use SE, scattered beam electrons, characteristic X-rays, and electron energy loss, signals that cannot be spatially correlated in TEM.

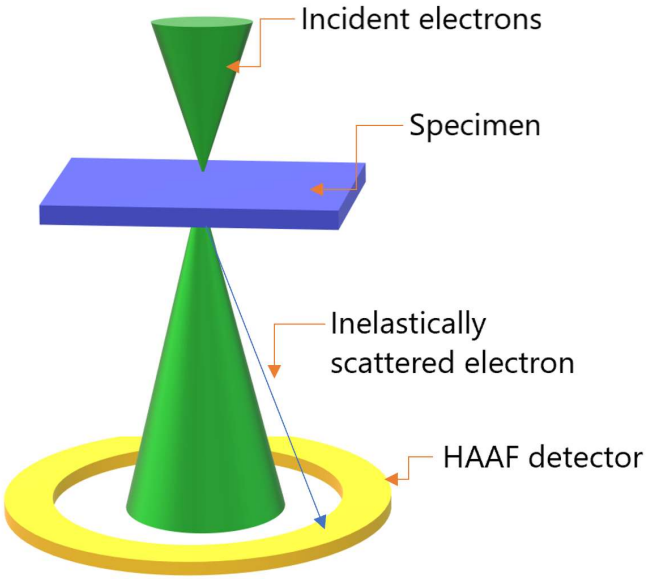

Figure 2.25 STEM schematic diagram.

Like SEM, STEM scans a fine, focused and rastered beam of electrons across the sample. Interactions between the beam electrons and sample atoms generate a serial signal stream, which is correlated with beam position to build a virtual image in which the signal level at any location in the sample is represented by the gray level at the corresponding location in the image. Its primary advantage over conventional SEM imaging is the improvement in spatial resolution.

Scattered beam electrons. Beam electrons may be elastically scattered by the nuclei of sample atoms. In a bulk specimen in a SEM, elastically scattered beam electrons that have been directed back out of the sample constitute the backscattered electron (BSE) signal. In STEM, transmitted beam electrons that have been scattered through a relatively large angle are detected using a high angle annular dark field (HAADF) detector. HAADF detector can also be used for grain morphologies imaging and Z-contrast.

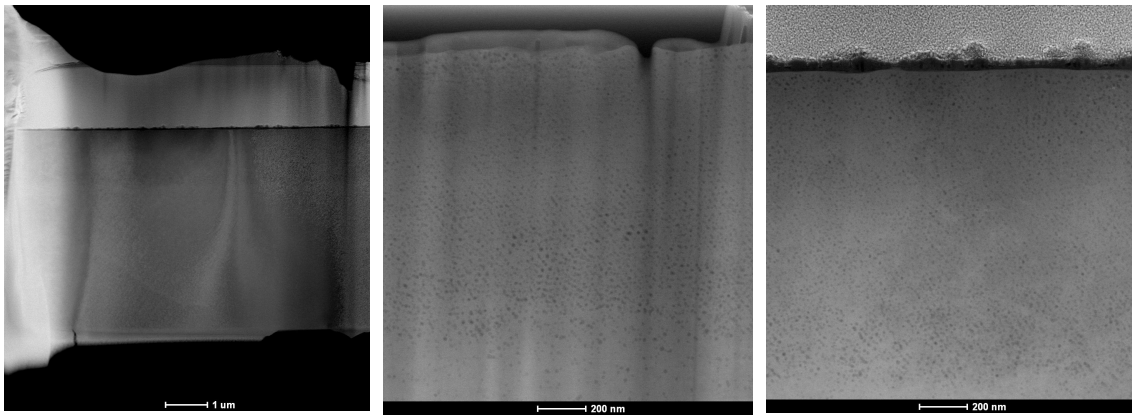

Figure 2.26 Typical STEM images taken form Cr sample.

2.3.4. EELS sample thickness measurement

Electron energy loss spectroscopy (EELS) provides quick and reliable measurement of TEM lamella thickness, which is needed for swelling calculations in this study. When known energy of electrons lose their energy while interacting with specimen by inelastic scattering, those energy losses can be measured by electron spectrometer and the peaks can be distinguished from each other.

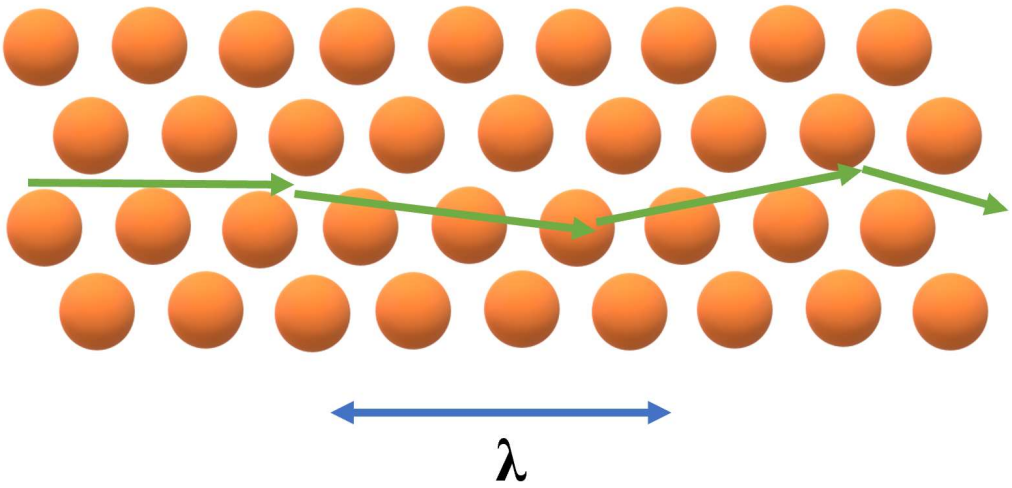

Figure 2.27 Electron inelastic mean free path in the specimen.

The inelastic mean free path λ is the mean distance between inelastic scattering events for these electrons. For random inelastic scattering event, the probability of n-fold inelastic scattering follows a Poisson distribution.

$$P_n = \frac{I_n}{I_t} = \frac{\left(\frac{t}{\lambda}\right)^n}{n!} e^{\left(-\frac{t}{\lambda}\right)} \qquad \text{Eq. 2.2}$$

where

t – specimen thickness

λ – mean distance between inelastic scattering events

n – number of inelastic scattering events,

I_n – intensity of n-fold scattering,

I_t – total intensity.

For n=0,

$$\frac{t}{\lambda} = -ln\left(\frac{I_0}{I_t}\right) \qquad \text{Eq. 2.3}$$

where

- I_o - intensity of 0-fold scattering (the elastic scattering signal).

This method is known as **the log-ratio method,** it is the most popular tool of thickness measurements by EELS. From a spectrum, the integral of the zero-loss peak (ZLP) will give I_o, while the integral of the entire spectrum will give I_t (Figure 2.28).

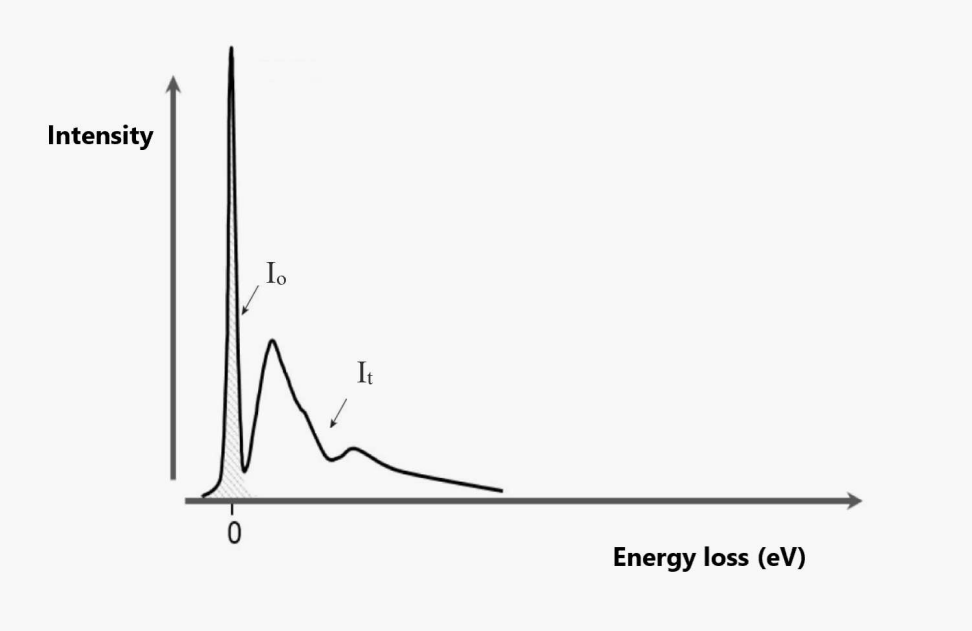

Figure 2.28 Log-ratio method for sample thickness measurement.

Two variants of this method are used ‘‘log-ratio (relative)’’ and ‘‘log-ratio (absolute)’’. Relative method uses only an assumption that scattering events have independent nature, so a simple expression Eq. 2.3 is used for thickness calculation. This method is easy and reliable, though relative.

Absolute measurements with the log-ratio method require knowledge of the mean free path of inelastic electron scattering k, which is strongly dependent on the material and the measurement conditions. Additional information needs to be input, like material Z-number, energy used, etc.

2.3.5. Focused Ion Beam (FIB) Lamella Preparation

Tescan LYRA-3 at Texas A&M Materials Characterization Facility (MCF) shown on Figure 2.29 is a powerful FIB instrument as it is combined with a SEM as a DualBeam system.

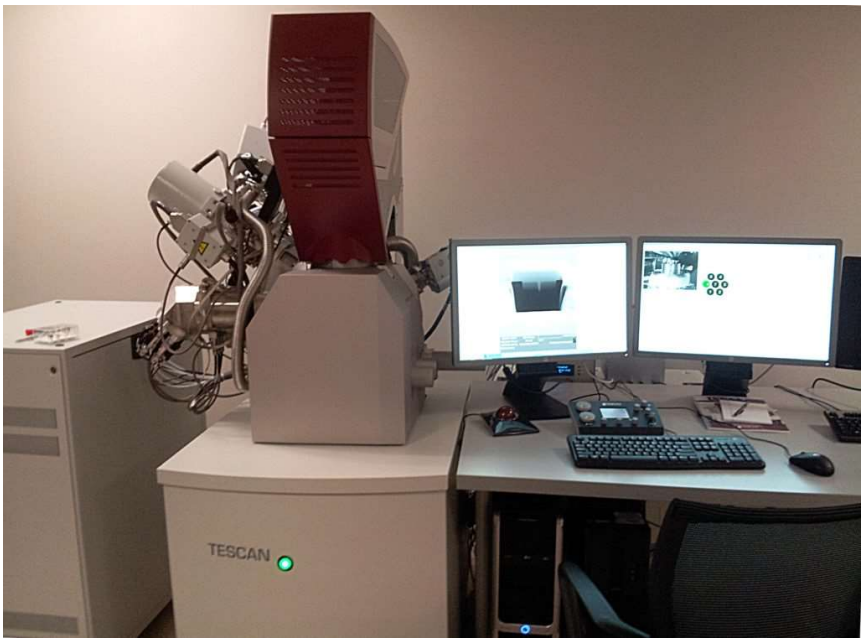

Figure 2.29 Tescan LYRA-3 Model GMH FIB Microscope at Texas A&M MCF.

In LYRA-3 the electron and ion beams intersect at a 55° angle at a coincident point near the sample surface, allowing high resolution SEM imaging of the FIB-milled surface. LYRA is additionally equipped with precursor-based gas injection systems (GIS) and nanomanipulator that helps to prepare TEM specimens with ultrahigh precision (Figure 2.30).

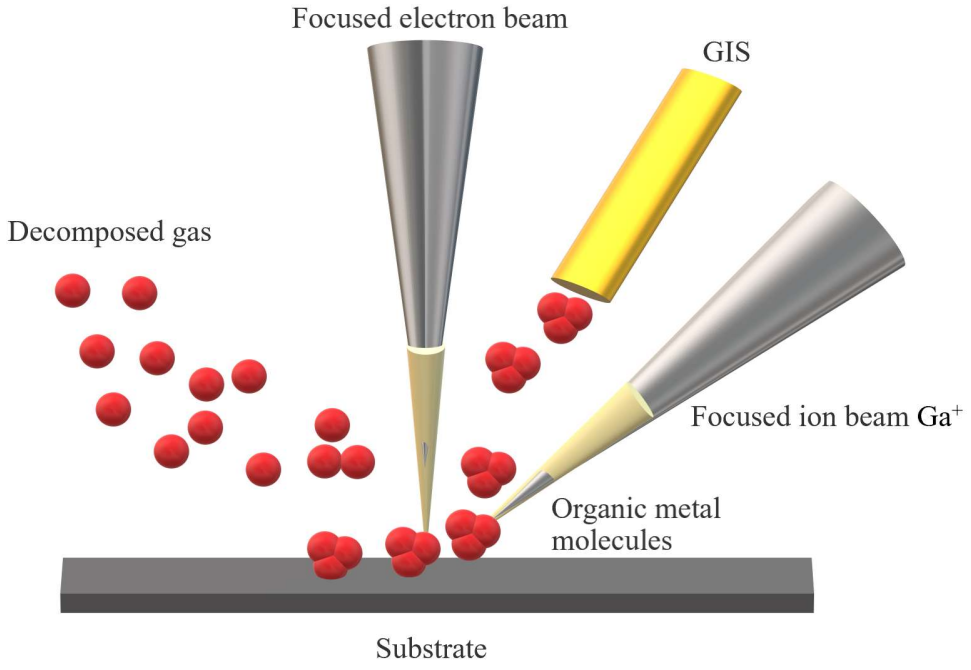

Figure 2.30 The typical dual-beam column configuration of vertical electron column, tilted ion column and GIS.

In FIB-SEM LYRA-3 system, liquid metal ion source (LMIS) generates a focused beam of metal ions of about ≈5 nm in diameter, and ion source contains a tungsten (W) needle attached to a reservoir that holds the metal source material. FIB-SEM LYRA-3 uses gallium (Ga^+) as a commonly preferred metal. Gallium's melting point is very low (T_m =

29.8 °C), that helps to minimize reaction between liquid metal and tungsten needle, which emits ions.

FIB column is responsible for producing and directing a beam of a relatively large element ionized atoms (Ga^+ ions) of high energy. Once ions are extracted from the source, they are accelerated up to 30 keV and later focused using electrostatic lenses – condenser and objective lenses. The condenser lens in responsible for probe-forming and objective lens focuses the beam at the sample surface. Focused beam is used for etching or milling sample surface or imaging.

Greater mass (like Ga^+) is important for ions as it helps them expel surface atoms from their locations to produce secondary electrons. SE allow ion beam to image sample before, during and after surface milling process. Ion beam also is used for material deposition from gaseous layer above the sample (Figure 2.30).

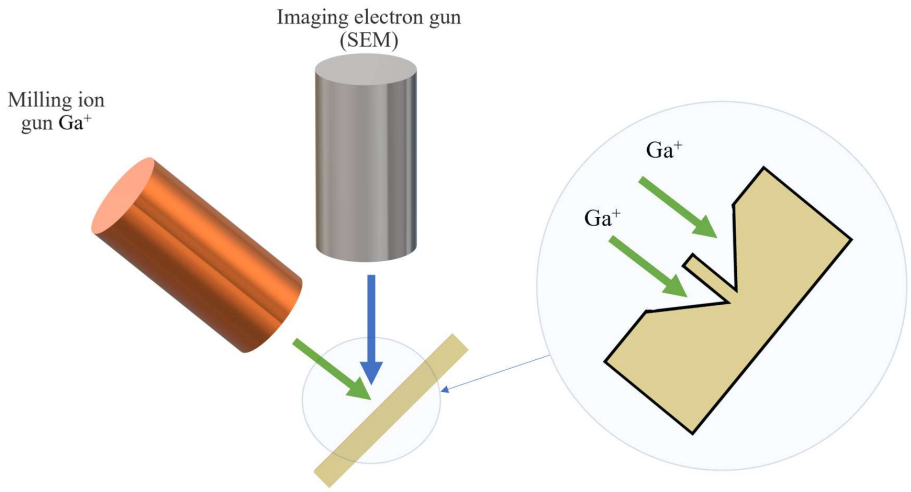

Figure 2.31 FIB-SEM dual system scheme for milling and imaging.

FIB dual system is one of the best techniques for TEM specimen preparation (Figure 2.31). For an efficient TEM analysis the specimen must be very well manufactured so it can

represent all the properties of the bulk material at the nanometer scale. FEB-SEM LYRA-3 uses ion milling with Ga^+ ions, Pu deposition for surface protection, manipulation, welding and polishing.

Deposition is a process of adding material on the specimen surface (Figure 2.35 b). Deposited material (like C, Pu) is released by GIS in a form of a chemical compound - organometallic molecules. Those molecules are released very close to the sample surface and when bombarded by focused ion beam, become decomposed, depositing almost pure material on the surface in a needed shape and form to protect material beneath deposited layer. Ion milling is a process of continuous sputtering produced by ion beam hitting the sample surface. Speed of material removal depends on the beam current and voltage. Milling specifically used for trenching (Figure 2.35 c).

- **TEM specimen preparation**

For the current study dual-beam instrument was used for preparing TEM lamellae that are thin enough to be transparent for electrons. TEM specimens were prepared with the "in situ lift-out technique," in which micromanipulator unit, placed in the microscope chamber, transfers the lamella to the TEM grid (Figure 2.32).

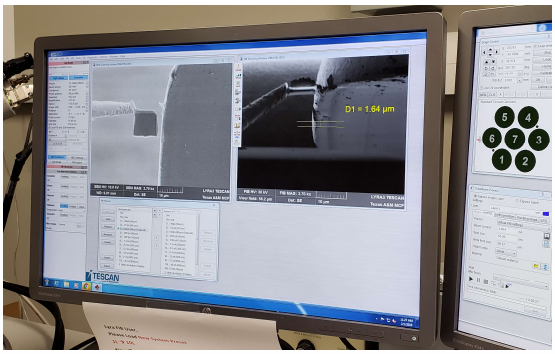

Figure 2.32 FIB-SEM micromanipulator in use for transferring Cr lamella to the TEM grit.

In this procedure, after grain selection, platinum (Pu) protection layer is placed on the region of interest using beam-induced deposition with milling away two trenches, leaving behind a 1–2-µm-thin section (Figure 2.33 a-c). This step can be named as "pre-lamella".

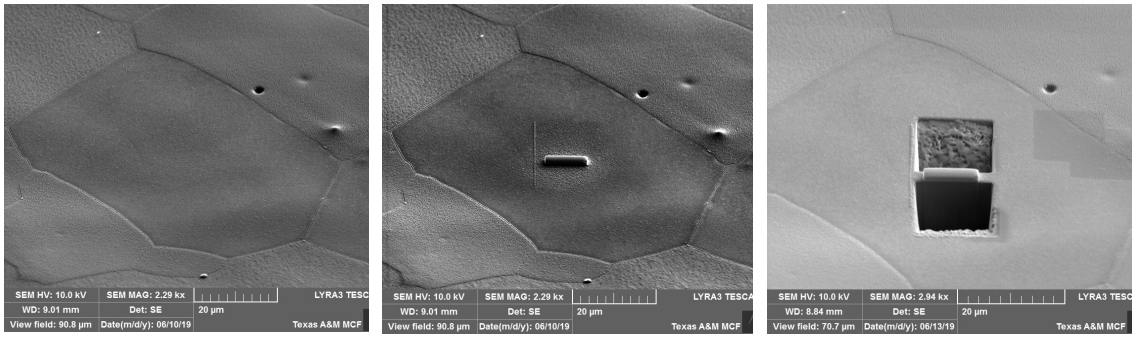

a. Grain selection b. Platinum deposition c. Digging two trenches

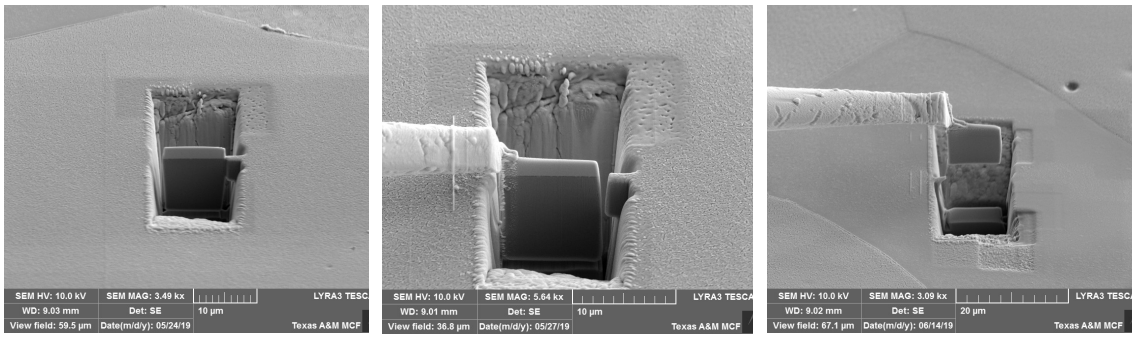

d. C-section e. Manipulator welding f. Lift-out

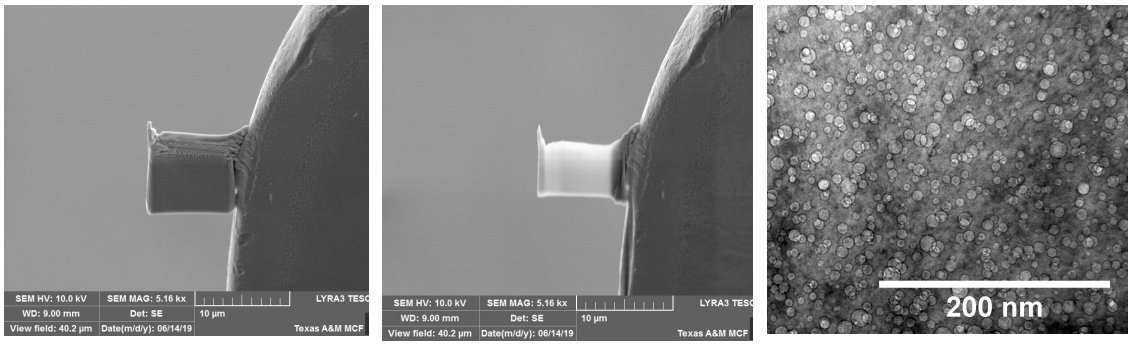

g. TEM grit mounting h. Lamella thinning i. TEM image of lamella

Figure 2.33 SEM images of TEM lamella lift-out process.

The next step involves cutting the bottom part and the side trenches away, until the section is held by the bulk sample from its shoulders – so call "C-section" (Fig. 2.33 d). Then, this pre-lamella can be welded to the micromanipulator using platinum deposition and cutting away the shoulders, and can be lifted out from the sample, transferred, and welded to a TEM grid (Fig. 2.33 e-f).

Afterwards, final thinning and polishing down to a thickness of < 100 nm is achieved using low incident angles and low ion currents (Fig. 2.33 h). Finally, the sample is ready for TEM analysis (Fig. 2.33 i).

2.3.6. Void swelling in metals under irradiation

Void swelling represents the volume change of nuclear materials under irradiations. Void swelling was first observed in the late 1960s in austenitic SSs irradiated in fast reactors to neutron exposures [6]. Using TEM, Cawthorne and Fulton [7] demonstrated that swelling in SS was due to the formation of small cavities within the grains of the alloy. Observed voids did not contain gas, so couldn't be classed as bubbles, and their sizes ranged from the smallest to greater than 1000 Å.

It is well known now that materials under irradiation are damaged by atoms being displaced from their lattice position. Those displacements create point defects - vacancies and interstitials, most of which are annihilated by recombination. Small portion of surviving defects causes changes in the metal microstructure by rearranging into more stable configurations.

Interstitials produce large strain field around them, that leads to a strong interaction between interstitials and dislocations. This interaction produces a preferential migration of interstitials toward dislocations, leaving some vacancies behind. Those remaining vacancies

do not have enough interstitials to annihilate with by recombination. Point defects uneven movement leads to the nucleation of cavities.

These cavities under specific temperature and dose rate for a material, eventually grow to much larger sizes. However, the main fundamental driving force of void formation is the excess of non-recombined vacancies movement toward voids. **"Void swelling"** occurs when large number of voids are formed causing an increase in the volume of the material.

Conditions necessary for void swelling in metals are [8]:

1. Both point defects, interstitials and vacancies, must be mobile in the solid.

2. Point defects must be capable of being removed at sinks provided by structural defects in the solid in addition to being destroyed by recombination.

3. The supersaturation of vacancies must be large enough to permit voids and dislocation loops to be nucleated, either homogeneously or heterogeneously, and to grow.

4. Trace quantities of insoluble gases must be present to stabilize the embryo voids and prevent collapse to vacancy loops. Gaseous impurities (oxygen, nitrogen, and hydrogen) present in most metals can perform this function.

2.3.6 Void swelling calculation method

Information on void swelling in metals is usually obtained by transmission electron microscopy (TEM). This technique is used to calculate the void distribution function, N(R)dR = number of voids per cm^3, where R is void radii between R and R + dR. Formulas used in the study:

Total void number density:

$$N = \int_o^\infty N(R)dR, \qquad \text{eq. 2.4}$$

Average void size:

$$\bar{R} = \frac{1}{N}\int_0^\infty R\, N(R)dR, \qquad \text{eq. 2.5}$$

Void swelling:

$$\frac{\Delta V}{V} = \frac{4}{3}\pi \int_0^\infty R^3 N(R)dR. \qquad \text{eq. 2.6}$$

To be sure that all calculations for all samples are made in the same way, unified void measurement method was used.

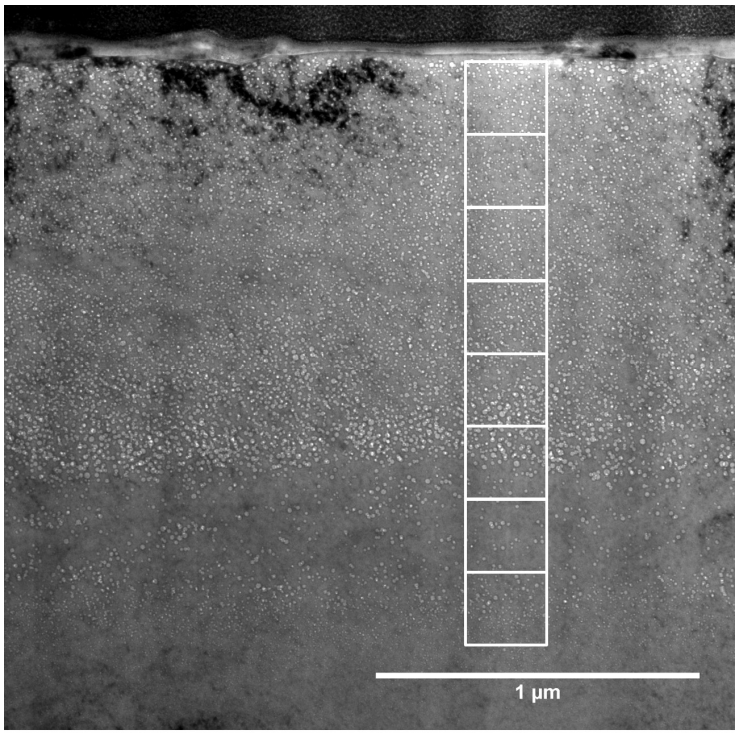

Figure 2.34 Scheme of TEM images taken for void swelling calculation.

- Due to intense swelling and small voids diameter in Cr high magnification images were used – 71k.
- To obtain good statistics average 200 voids is needed in 100 nm region, 71k magnification provides an image 312.55 nm by 312.55 nm.

- Average 3000 voids are measured in each sample for a full range calculation – up to 2 micron depth.
- With this method it is possible to see and measure every single void with a very little error.

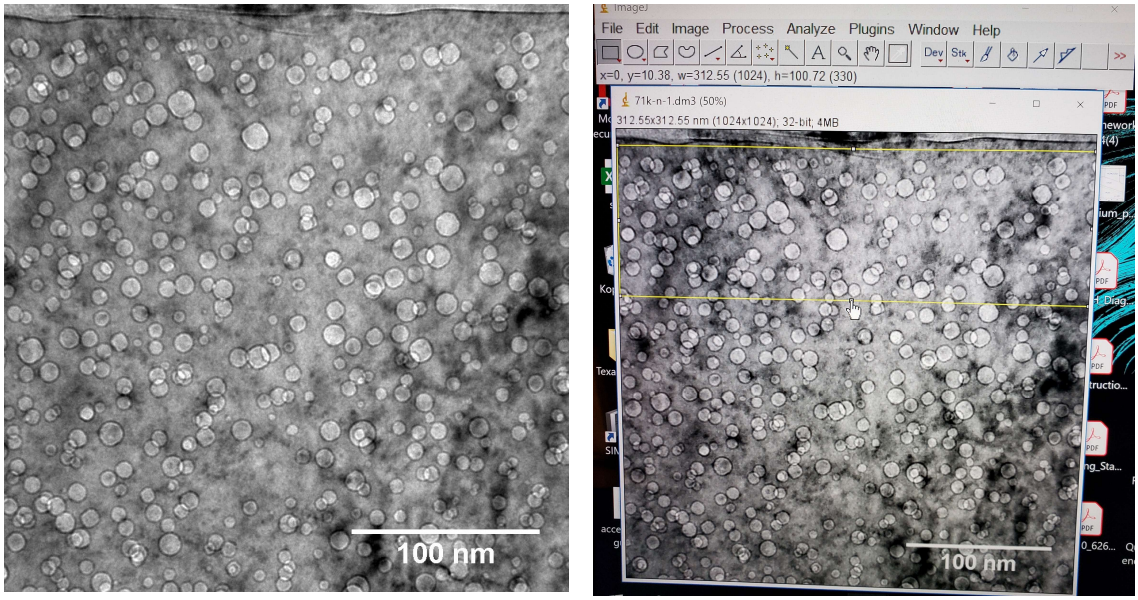

Figure 2.35 a) Typical TEM image of Cr sample used for voids measurement, b) Process of image cutting for detailed voids measurement.

Figure 2.35 b shows ImageJ software used to cut each TEM image into images of size 312.55 nm (width) by 100 nm (depth). For each 100 nm portion of the original TEM image every void's diameter is measured.

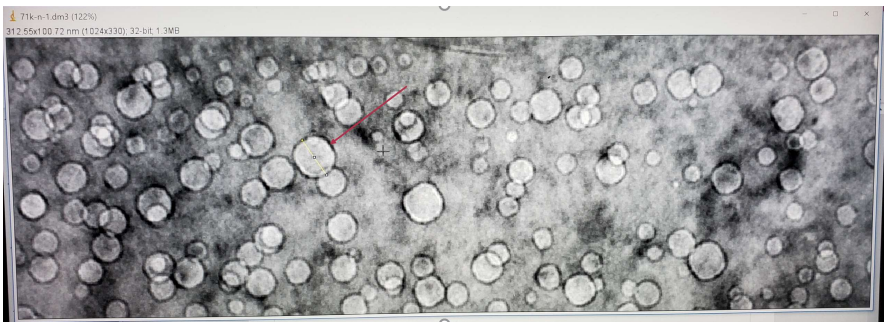

Figure 2.36 Voids diameter measurement technique.

To calculate total void swelling lamella thickness is needed, thickness was measured using EELS in two regions (Figure 2.37):

1) From 0 to 800 nm (top),

2) From 800 to 1600 nm (bottom).

During FIB thinning lamella is made of uneven thickness, much thinner on the top. To have precise swelling calculation, average thickness is used for full range swelling, and for 200-600 nm range only upper part.

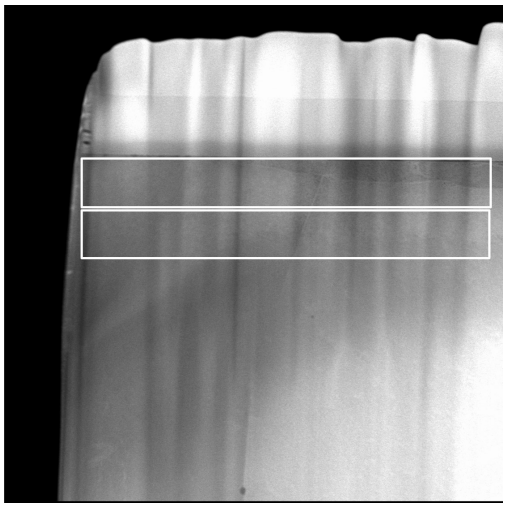

Figure 2.37 EELS Cr lamella's areas used for thickness measurement.

2.4 References

[1] L. A. Alasagas at al., USNA Pelletron accelerator applications with heavy ion projectiles. Nuclear Engineering and Design. 338: 1-4. 2018.

[2] J.G. Gigax et al., The influence of ion beam rastering on the swelling of self-ion irradiated pure iron at 450 °C, Journal of Nuclear Materials 465, 343-348 (2015).

[3] L. Shao et al., Standardization of accelerator irradiation procedures for simulation of neutron induced damage in reactor structural materials, Journal of Nuclear Materials 409, 251-254 (2017).

[4] J.G. Gigax et al., Beam-contamination-induced compositional alteration and its neutron-atypical consequences in ion simulation of neutron-induced void swelling, Mat. Res. Lett. 5, 478-485 (2017).

[5] Malis, T.; Cheng, S. C.; Egerton, R. F. EELS log ratio technique for specimen-thickness measurement in the TEM. J. Electron Microscope Technique. 8:193; 1988.

[6] O. K. Chopra, A. S. Rao, A review of irradiation effects on LWR core internal materials - Neutron embrittlement, void swelling and irradiation creep, Journal of Nuclear Materials, Volume 412, Issue 1, p. 195-208. 2011

[7] CAWTHORNE, C., FULTON, E. Voids in Irradiated Stainless Steel. Nature 216, 575–576 (1967).

[8] Olander, D.R. Fundamental aspects of nuclear reactor fuel elements. United States: N. p., 1976.

3. TEMPERATURE AND DPA STUDY ON PURE CHROMIUM VOID SWELLING*

3.1. Introduction

In the current study the Texas A&M 3.0 MV accelerator was used to obtain an expanded understanding of the temperature, dose and dose rate dependence of void swelling in pure chromium. It was also desired to explore the depth dependence of swelling over the full ion range. At this point it is not certain whether neutron-induced swelling will occur at PWR-relevant temperatures nor is it certain whether there is a strong temperature dependence of the post-transient swelling rate that would require the use of a temperature shift associated with the much higher-than-neutron dpa rate used in the ion simulation.

However, the strong oxide-forming nature of chromium poses a problem for ion simulation of swelling in our accelerator facility. Ideally, Cr self-ion irradiation is the best choice for high levels of damage introduction into pure chromium, but Cr ion beam production using SNICS (Source of Negative Ions by Cesium Sputtering) is very weak with unstable ion current, largely due to its strong oxygen affinity. Therefore, in the present study, 5 MeV Fe^{2+} ion irradiation was performed to study the swelling dependence on damage level, dpa rate and irradiation temperature, as the first step to evaluate the irradiation performance limitations of chromium coating.

In contrast to the previous studies : (1) 5 MeV Fe ions were used to create a much deeper depth profile; (2) the void depth dependence was extracted using FIB-produced

* Reprinted with permission from "Irradiation-induced swelling of pure chromium with 5 MeV Fe ions in the temperature range 450–650 °C" by Ekaterina Ryabikovskaya, Aaron French, Adam Gabriel, Hyosim Kim, Tianyao Wang, Koroush Shirvan, Frank A. Garner, Lin Shao, 2021. *Journal of Nuclear Materials*, Volume 543, Copyright 2020 by Elsevier.

lamella to evaluate the influence of the free surface, injected interstitial and depth-dependent changes in dpa rate; (3) the irradiation temperature range was chosen to be 450–650°C, searching for the swelling peak at 50 dpa; (4) and finally, at the maximum swelling temperature of 550°C observed at 50 dpa, irradiation was conducted to doses of 100 and 150 peak dpa to obtain a swelling rate over a wide range of displacement dose.

3.2. Experimental Procedure

The study included two sets of experiments. First, a temperature dependence study was conducted in which irradiation proceeded to 50 peak dpa at temperatures of 450°C, 500°C, 550°C, 600°C, and 650°C where the outer temperature limits were determined by probing for those temperatures where swelling was falling strongly. The second set was a dose dependence study in which the temperature was fixed at 550°C (once it was determined to be the maximum swelling temperature in the previous irradiation set) and irradiation then proceeded from 50 to 100 and 150 peak dpa. The Stopping and Range of Ions in Matter (SRIM) code was used for damage calculation [1]. The Kinchin-Pease mode with a Cr displacement energy of 40 eV was used as suggested by Stoller et al. [2]. The peak dpa rate was 1.7×10^{-3} dpa/sec. for a beam current of 200 nA over an area of 6mm×6mm.

Bright field transmission electron microscopy (TEM) and scanning transmission electron microscopy (STEM), with a high angle annular dark field (HAADF) detector on a FEI Tecnai F20 ST with an operating voltage of 200 kV, were used to characterize microstructures. Focused ion beam (FIB) lift-out technique was used to prepare TEM specimens. Thickness of each TEM lamellae was measured using a standard electron energy loss spectroscopy (EELS) on the FEI Tecnai F20 equipped with a Gatan imaging filter. All the used equipment and techniques are described in Section 2.

Figure 2 shows that the maximum range of Fe ions is ~1.8 μm with a peak in the implanted distribution at ~1.5 μm while the dpa damage distribution peaks at ~1.2 μm. Normally one would avoid swelling data collection in the implanted region to avoid complexity from injected interstitial suppression, but in this case we must also avoid the implantation-induced composition change, reaching a peak level of ~4% Fe at 150 dpa. Therefore, the region shallower than 700 nm was used to determine the swelling behavior, but as shown later, there is value in considering the full range swelling distribution.

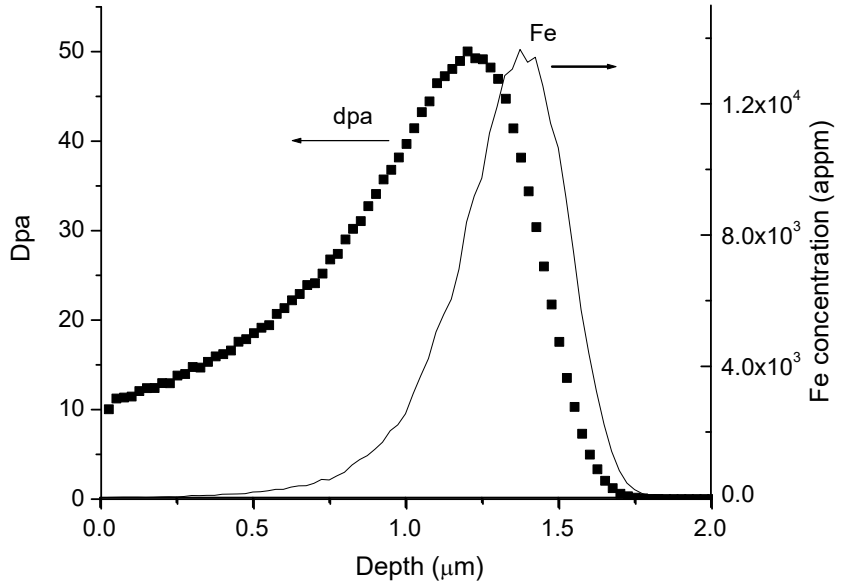

Figure 3.1 SRIM-predicted distributions of dpa damage and Fe implantation, caused by normal-incidence 3.5 MeV Fe ions into pure chromium, for a dose corresponding to 50 peak dpa.

3.3. Results

Figure 3.2a shows a cross-sectional TEM micrograph of pure chromium irradiated at 50 peak dpa and 550 °C. Superimposed are SRIM-predicted dpa and implant profiles. There are several interesting observations: (1) As shown in Figure 3.2b, there is no noticeable void

depletion near the surface. A high density of voids exists immediately beneath the surface. This is very different from other bcc metals such as Fe where a surface void depletion zone of ~200 nm is typical [3]. (2) As shown in Figure 3.2c, there is no obvious void depletion in the deposited Fe range. This is very different from most pure metals and alloys, in which injected interstitials almost always suppress void formation completely in this region [3, 4, 5-10]. (3) As shown in Figure 3.2d, however, void depletion along grain boundaries was observed, as is universally observed in hundreds of previous swelling studies on many metals. The difference in denuding behavior between the surface and grain boundaries will be addressed later.

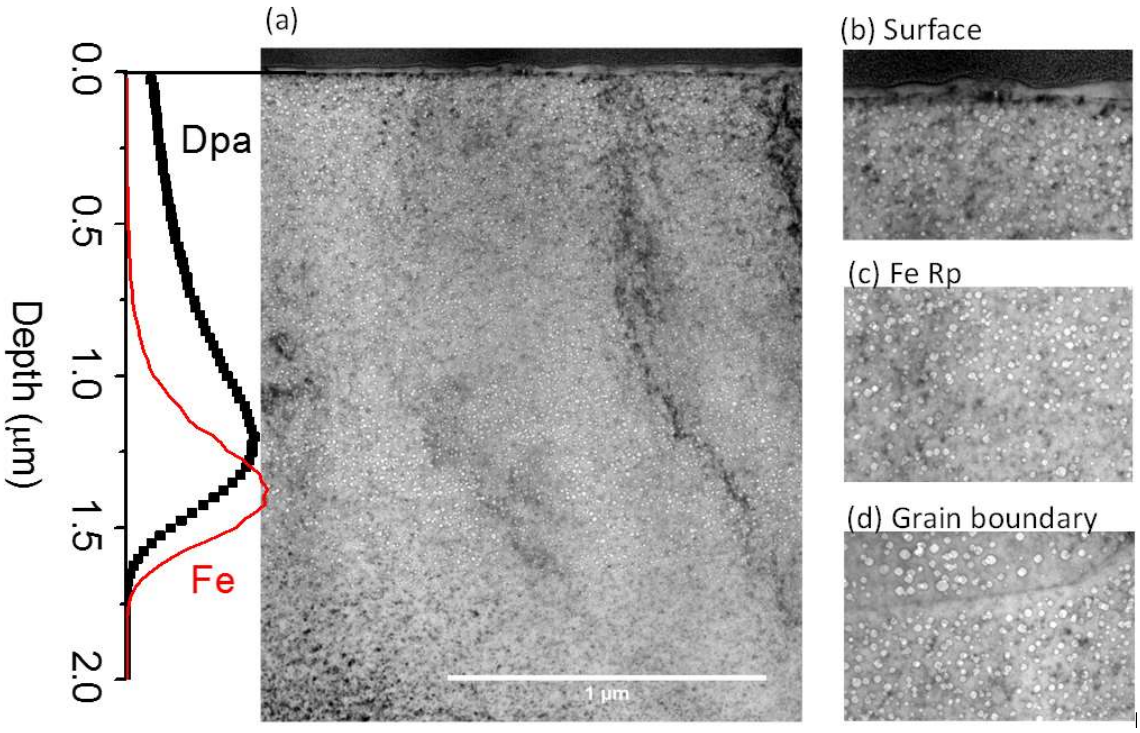

Figure 3.2 (a) Cross-sectional TEM image of pure chromium irradiated to 50 peak dpa at 550°C. Superimposed are SRIM-predicted dpa and implant profiles. Higher magnification images from (b from the near surface region. (c) near the Fe mean projected range, Rp. (d) a region containing a grain boundary.

One very important finding in the present study is that voids in Cr are becoming progressively aligned with increasing dose. If one looks closely at Figure 3.2a a developing tendency for void alignment can be seen in the 50 peak dpa specimen. Lines of voids can be seen with your eyes moving from left to right at an upward angle of ~15-20°. Figure 3.3a shows a clearer image of ordering in the 100 peak dpa specimen at 550°C. Due to a fortuitous choice of grain for FIB production voids are aligned along the vertical direction in the imaged grain in this specimen. This figure also shows two consequences of the ion path crossing a grain boundary. There is a void denuded zone on each side of the grain boundary and the aligned void arrays change direction when crossing into the lower grain. As additional evidence of better visualized ordering, Figure 3.3b shows an enlarged STEM image under optimized tilting. Voids appear as dark spots with roughly equal spacing, but the regularity is not yet completely established at this dose level. Similar void alignments were observed in other samples irradiated under different dose and temperature conditions. The ease of seeing void alignment is strongly dependent on the orientation of the foil with respect to the axes of the superlattice, best observed for imaging along the close-packed direction [111] and at higher dpa levels where the ordering becomes better established.

In order to further understand the alignment direction, we perform an EBSD scanning over Cr sample surface prior to FIB. Based on grain orientation information obtained from EBSD, we selected two grains to FIB lift out: one is [110] oriented and the other is [111] oriented. Figure 3.4 shows how under slight rotation adjustment, keeping $\beta=0$ and changing α, vertical void alignment easily appear (with the alignment direction along the surface normal direction). On the other hand, for [110] oriented grain, void alignment does not

appear when keeping β=0. These observations evidence that the void alignment direction is along [111] axial direction.

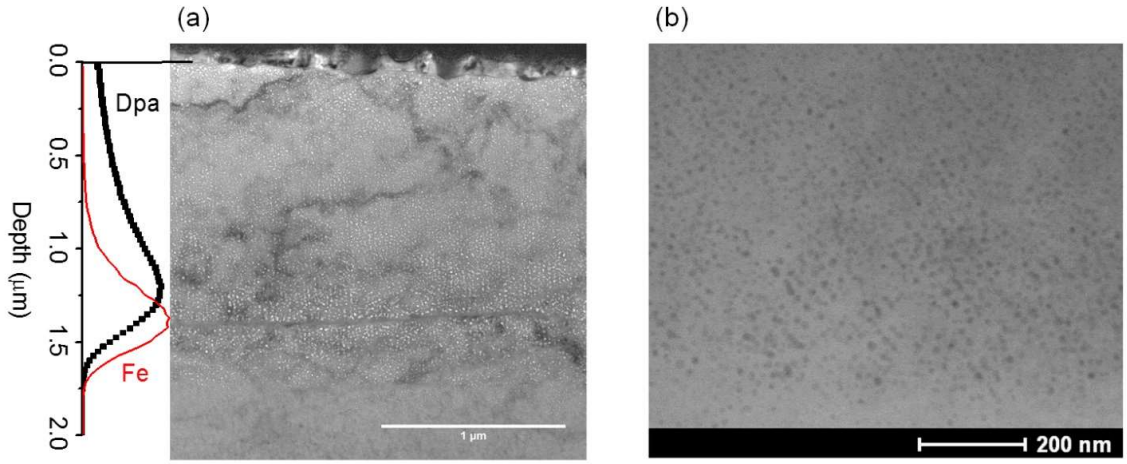

Figure 3.3 (a) Cross-sectional TEM image of specimen irradiated to 100 peak dpa at 550°C. Superimposed are the SRIM predicted dpa and implant profiles. (b) an enlarged STEM image showing void alignment.

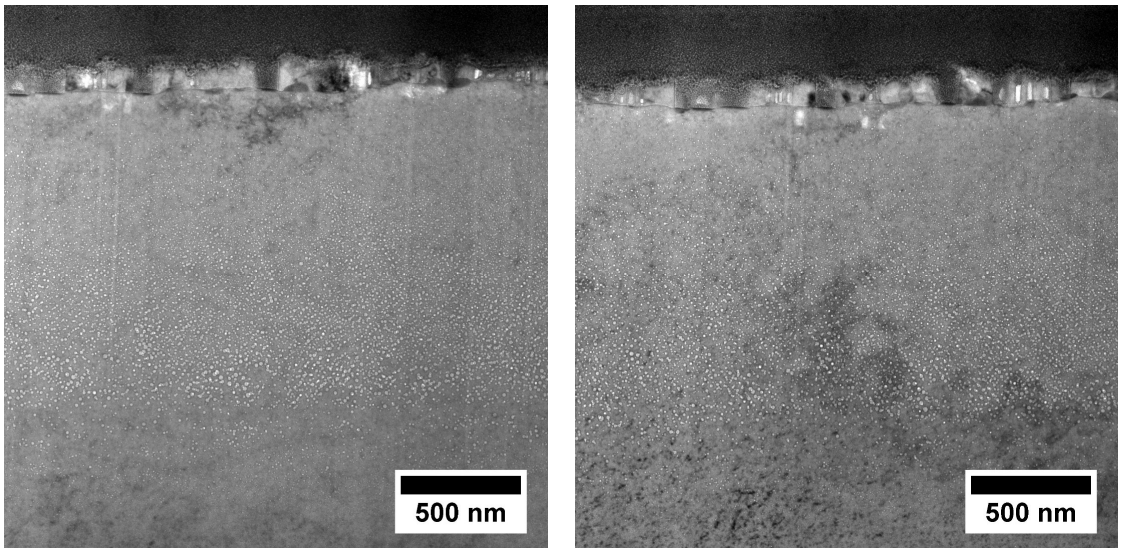

Figure 3.4 Cross-sectional TEM image of specimen irradiated to 100 peak dpa at 550°C showing void alignment of [110] oriented grain: a) tilted at angles α = 12.7 and β = 0, b) tilted at angles α = -16.9 and β = 0.

Void superlattices and gas bubble superlattices have been reported in many metals under gas ion implantation, heavy ion irradiation, and neutron irradiation as summarized in various review articles [11-14]. Although a bubble superlattice has been previously observed in chromium [14], this is the first time in open literature that chromium has been seen to develop a void lattice, although Ukrainian work [15] contains and briefly discusses one micrograph showing void ordering.

We now proceed to examine both the temperature and dpa dependence of swelling. Figure 3.5 shows that the swelling does not vary strongly with depth at 50 peak dpa in the depth range <600 nm but does have a quite discernible dependence on temperature. Figure 3.6 presents the swelling at 50 peak dpa, averaged over the depth region of 200 to 700 nm, as a function of irradiation temperature. Note that this depth region has insignificant composition change due to injected Fe atoms. The maximum swelling is observed at 550°C, but it cannot be determined from these data alone whether this temperature dependence represents variations in either the transient duration or the post-transient swelling rate or possibly a combination of both. Note that this peak swelling temperature is higher than that of pure Fe and Fe-based ferritic alloys (~475 °C) previously conducted at Texas A&M on the same accelerator at nominally similar irradiation conditions. Since the melting point of Cr is higher than that of Fe (1907 vs. 1538°C) this upward shift in peak swelling temperature is not unexpected since swelling is known to be best described using homologous temperatures.

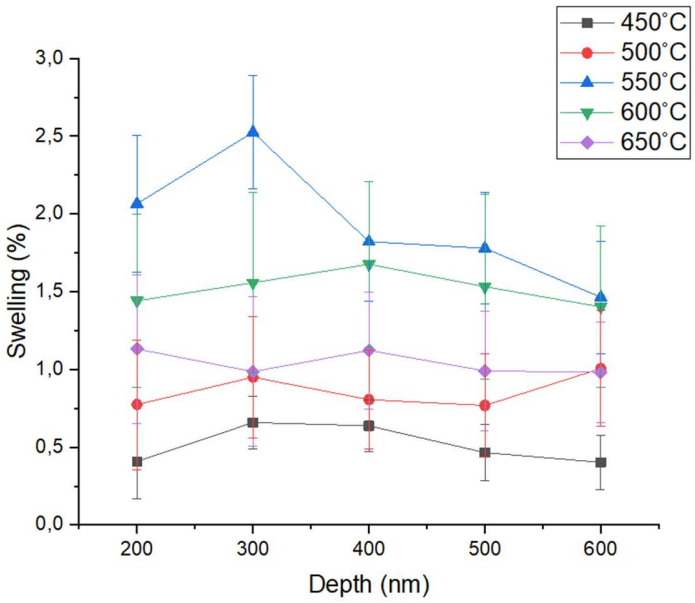

Figure 3.5 Depth-dependent swelling at 50 peak dpa, measured in the depth region <600 nm to avoid injected interstitial and Fe contamination effects.

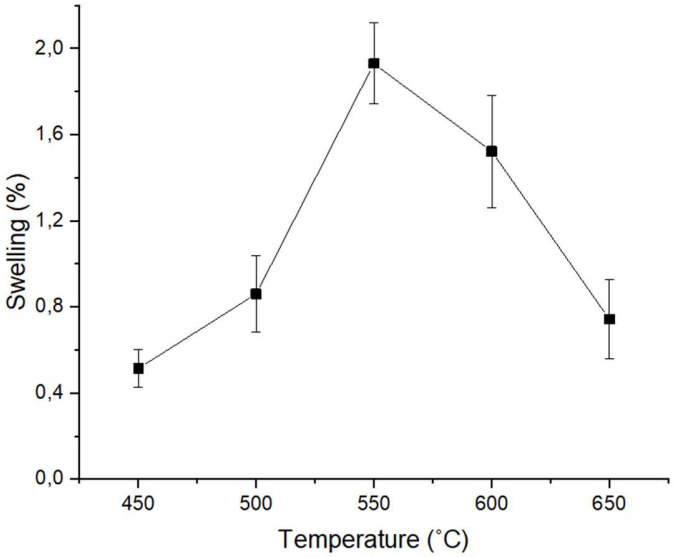

Figure 3.6 Void swelling of 50 peak dpa irradiated Cr, as a function of irradiation temperature. Swelling values presented here are averaged over the 200 nm to 700 nm depth range to minimize the influence of both the surface and the implanted ions.

The void densities at 50 dpa are roughly the same at all temperatures. The most dramatic changes are seen in the void diameter, as shown in Figure 3.7. From 450 to 550 °C, void diameters increase from ~4 nm to ~8 nm. From 550 °C to 650 °C, the void diameter decreases from ~8 nm to ~7 nm.

After 550 °C was determined to be the maximum swelling temperature in this experimental series, specimens were irradiated to higher doses at this temperature. Figure 3.8a-c shows TEM images of samples after 50, 100, and 150 peak dpa irradiation at 550°C, respectively. Again, no obvious surface void depletion zone was observed. Figures 3.9a and 9b summarize the void diameter and density measurements at different peak dpa values.

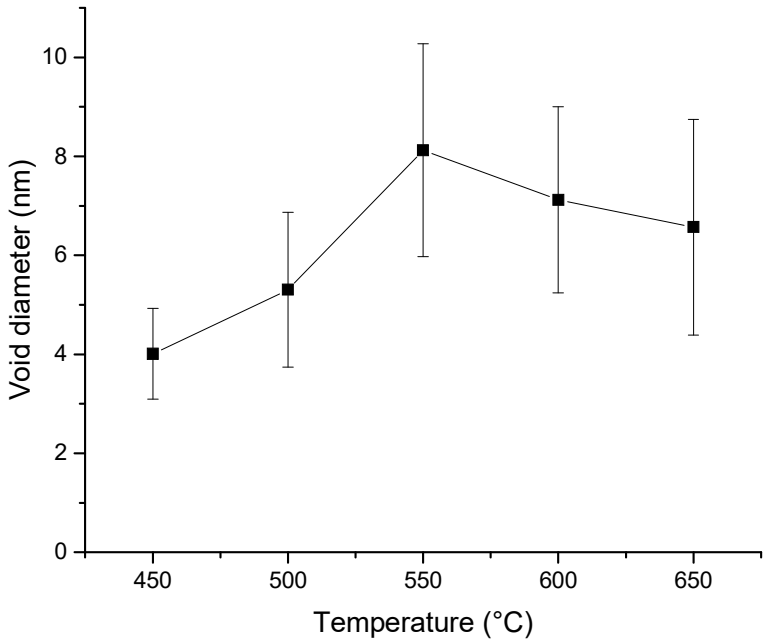

Figure 3.7 Void diameters of 50 peak dpa irradiated specimens, as a function of irradiation temperature. Size data presented here are averaged over the depth range of 200 nm to 700 nm.

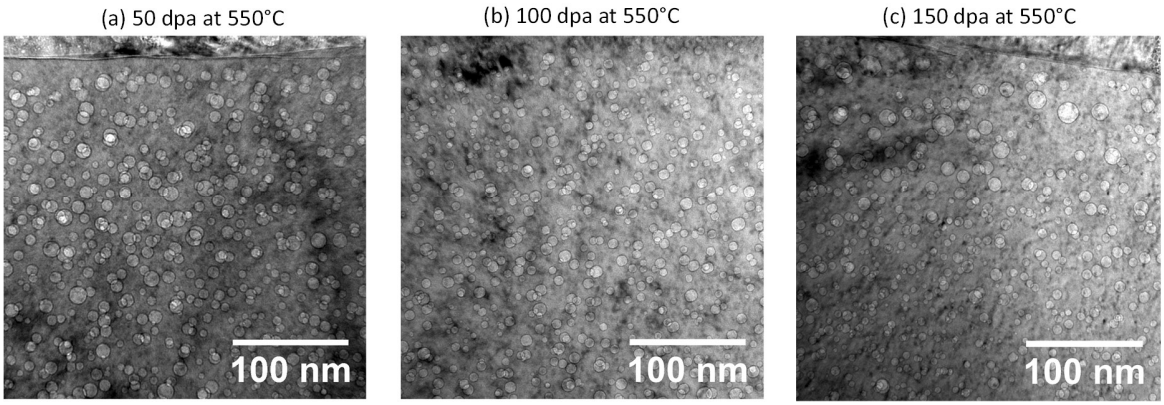

Figure 3.8 TEM micrographs of specimens irradiated to 50, 100, and 150 peak dpa values at 550 °C. The images were taken immediately beneath the surface.

The TEM cross-sectional images were divided into 100 nm wide bins to probe the depth dependence of swelling as a function not only of dpa but also dpa rate, the latter varying as a function of depth. As shown in Figure 3.9a, the void diameters increase with increasing damage levels, both as a general trend at different depths at one peak dose, and for the same depth at different doses. Note that the diameters did not show significant decreases at the peak injected range as one might expect due to injected interstitial suppression.

On the other hand, void concentrations do vary as a function of depth. As shown in Figure 3.9b, for depths <1000 nm with negligible Fe interstitial injection, the void densities increase with increasing dpa. In contrast, at ~1.4 μm, void densities are locally reduced to almost zero when peak dose values are larger than 50 dpa. It is obvious that the void density variations dominate the swelling variation with depth.

Figure 3.10a shows the SRIM-predicted Fe distributions for comparison with the depth-dependent swelling values shown in Figure 3.10b. The shadowed region around Rp marks the region of significant Fe interstitial injection. Swelling for 50 peak dpa shows small

variation as a function of depth, but at 100 and 150 dpa, swelling is greatly suppressed in the shadowed region. For the region shallower than 1000 nm, swelling increases with increasing local dpa.

After excluding the region affected by injected interstitials and their associated composition changes, we analyzed swelling as a function of dpa. Figure 3.11a plots the swelling over the depth region of 100 to 300 nm (in black) and also over the region of 400 to 700 nm (in red) at all three doses of 50, 100 and 150 peak dpa These two choices of depth range were made to see if there was an obvious difference between the two data sets arising solely from their difference in local dpa rate which is roughly a factor of 2.

Although there is some scatter, all data points in both sets appear to follow a line with slope of ~0.03% per dpa. Note that in many previous studies, swelling as a function of dpa for different depth regions often shows different behavior where dpa rate differences primarily affect the duration of the transient regime of swelling [16-18]. This suggests that swelling in this experiment is not very sensitive to dpa rate, especially since chromium shows an almost zero swelling incubation period. Based on this result Figure 3.11b was constructed that presents all depth-dependent swelling values for each depth bin for all three irradiation doses, without differentiation of the measurement depth or associated dpa rate. A linear dependence on local dose seems to be a good approximation with a slope of ~0.04% per dpa. In summary, there does not appear to be a discernible dependence of swelling in this experiment on dpa rate. Note also that the swelling curve in Figure 3.11b has a non-zero intercept at zero dose, implying that there is low dose transient at much higher swelling rate before the post-transient rate is established.

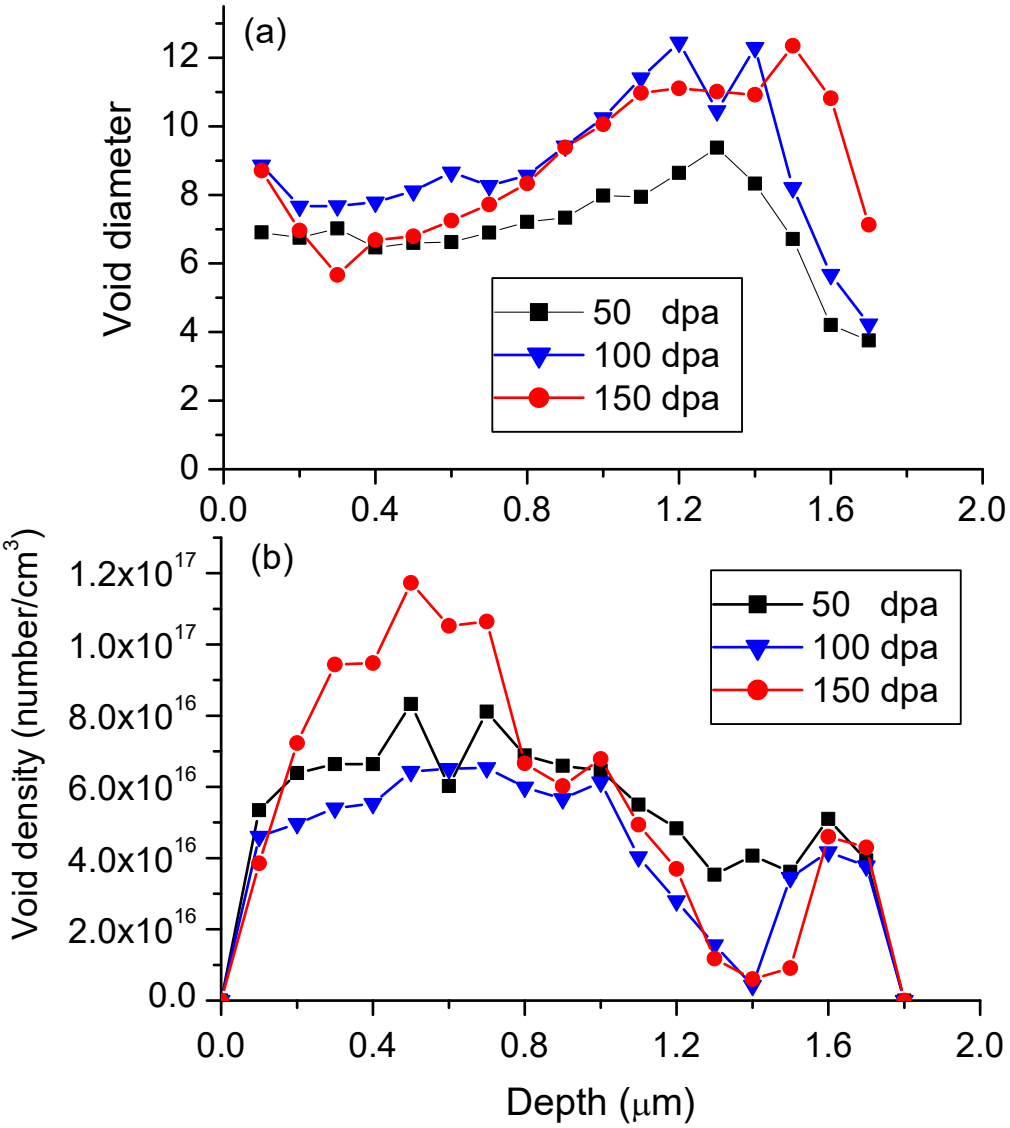

Figure 3.9 (a) Void diameters and (b) void densities as a function of depth after irradiation at 550°C to 50, 100, and 150 peak dpa.

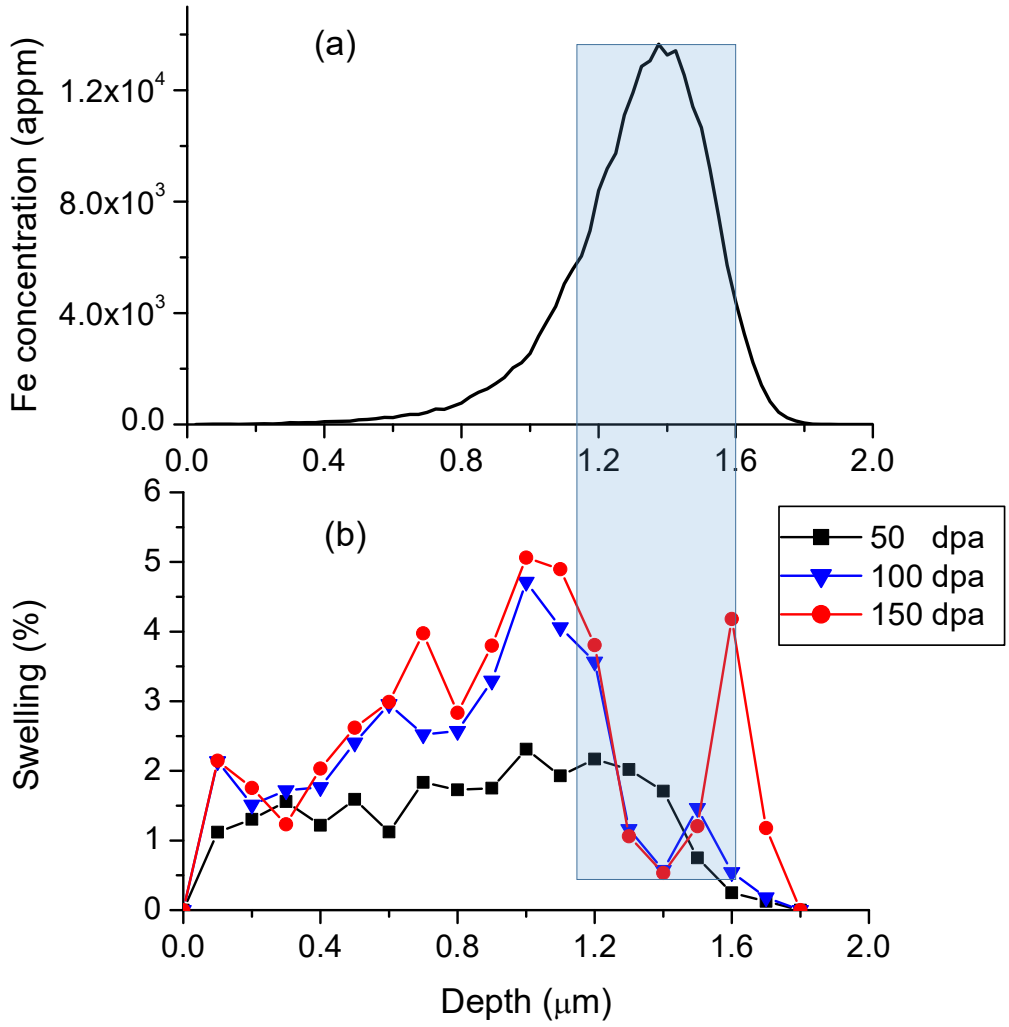

Figure 3.10 (a) SRIM-predicted Fe implant distribution for 50 peak dpa irradiation, and (b) swelling as a function of depth in pure chromium irradiated at 550 °C to 50, 100, and 150 peak dpa. The blue shadow box indicates the region of maximum compositional alteration by Fe implantation.

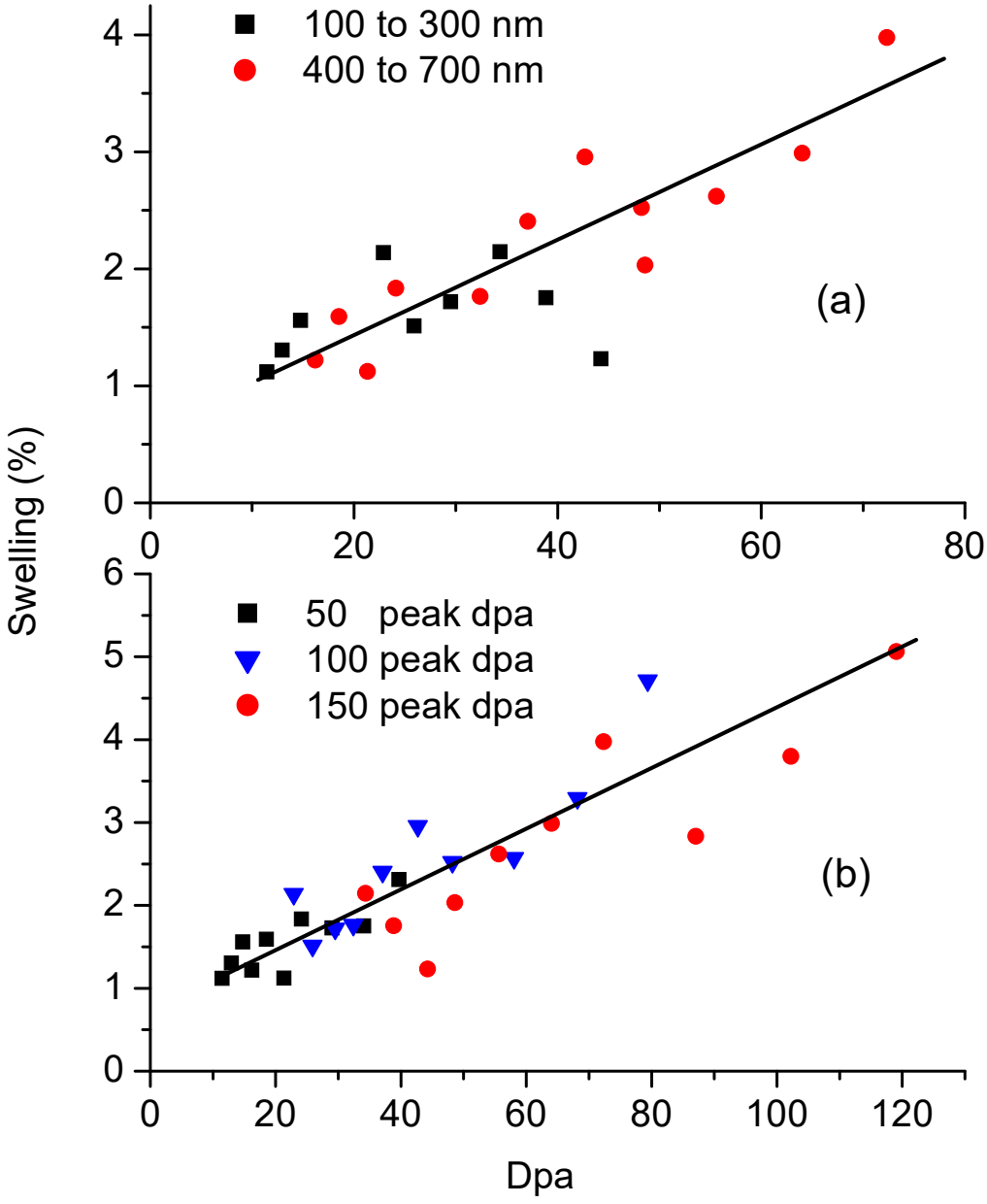

Figure 3.11 (a) Average swelling at 550°C as a function of local dpa for two depth regions, showing no strong sensitivity of swelling to the difference in average dpa rate. (b) Swelling in individual 100 nm bins below 700 nm, ignoring any differences in dpa rate, showing that swelling appears to be increasing with increasing dpa level almost everywhere but not is not sensitive to the local dpa rate.

3.4. Discussion

As discussed earlier the high dpa rates required to reach peak doses of 50-150 dpa could not be attained using a SNICS source of Cr ions in our accelerator, primarily due the strong tendency of chromium to bind with oxygen. Another consequence of the oxygen affinity appears to be the absence of void denuded zones at the ion-incident surface, even though internal grain boundaries were seen to develop the ubiquitous denuded zones always observed in other metals and alloys after irradiation to produce voids. Rate theory has suggested that for either a grain boundary or a free surface, void denuded zone formation can be described by two cases. If the bulk of the grain has a high efficiency for point defect recombination, the width of boundary void denuded zone can be estimated by $\Delta x \sim (\frac{D_V}{K})^{1/4}$, where D_V is the vacancy diffusivity and K is the damage rate. If the bulk defect recombination is weak, however, the width is proportional to $Cs^{1/2}$, where Cs is the sink density [19,20]. Both models require that the defect formation energy is lower at the boundary or surface. If void denuded zone forms around grain boundaries but not at the free surface, we hypothesize that the easy oxidation of chromium to form a very tenacious and impermeable oxide probably affects the defect sink strength of the surface and that this oxide coating is maintained in spite of ion-inducedsputtering at the surface, even at the high vacuum maintained in this experiment. It is well known that surface condition can sensitively change defect development [21].

Void formation behavior observed in this study and in the Russian/Ukrainian studies are remarkably similar, showing that chromium exhibited some unusual characteristics compared to other bcc metals. First, the post-transient rate was remarkably low compared another bcc metal such as alpha-Fe which swells at ~0.2%/dpa in both neutron and self-ion

irradiation [4, 33, 22, 23]. As a rule bcc metals are known to have lower post-transient swelling rates compared to fcc metals such as delta-Fe at ~1%/dpa [23, 25, 6] and copper at ~0.5%/dpa [26], but the rate of ~0.03-0.04%/dpa for bcc chromium is especially low.

Second, it appears that there is initially a higher transient swelling rate at very low dpa levels before settling down to the post-transient rate, as was observed in both the Ukrainian and Texas A&M studies. This behavior has been observed before in other pure metals, however and therefore is not so surprising. What is surprising, however, is that there appears to be an independence of the post-transient swelling rate, often referred to as the steady state swelling rate, on dpa rate over the factor of ~2 studied in this experiment. Perhaps these two items are linked in that the rate dependence in many studies on other metals and alloys was manifested primarily in the duration of the transient regime [16-18], which in the case of chromium is already near zero.

The absence of a dpa rate dependence adds some complication concerning the application of these data to light water reactor problems such as accident tolerance. In the present study and previous Russian/Ukrainian studies, void swelling was observed over a range of 400-850°C, all higher than the normal operating temperatures of Zircalloy cladding. There is no data below 400°C that provides insight on whether chromium might swell at PWR-relevant temperatures, but the observed range of the swelling temperature regime under both ion and neutron irradiation is very large.

The lack of total void suppression in the injected interstitial region at 25 dpa is another feature showing chromium to be different from other metals and alloys. Void suppression in this injected region has been a general phenomenon in almost all ion-irradiated metals, which is attributed to elimination of void nucleation by “excess”

interstitials. These excess interstitials arise from two combined effects. One is the spatial difference in vacancy and interstitial distributions, with the latter slightly being deeper than that of the former, leading to excess interstitials near the end of range [3]. The other is the extra atoms injected into this area due to implantation. However, note that 100 and 150 dpa there exists a local depression of swelling but not its complete absence. Perhaps the increasing local concentration of Fe atoms at these doses is involved, but this possibility requires additional study. Even in the presence of Fe it is obvious that chromium exhibits unusual behavior.

It is unclear whether void density shrinkage with increasing dose is caused by defect imbalance, or by fundamental defect kinetics changes in a region where the chemical composition is changed from pure Cr to dilute Cr-Fe alloys. Studies by Chen et al., although on α-Fe, has shown that Fe-Cr defect interactions can lead to a unique diffusion mechanism leading to long range migration of Cr [27].

While self-organization has not been observed in commercial structural alloys, it is well known that both pure fcc (Cu, Ni, Al) and bcc (Mo, Nb) metals and some dilute binary alloys can self-organize to develop dislocation loop lattices and walls, as well as void lattices and bubble lattices [11-14], and it appears that chromium is no exception with respect to bubble and void lattice formation. Bryk did not provide any evidence of loop lattices, but he noted that loops persisted to very high dpa levels, behavior not usually observed in structural alloys. For bcc metals these superlattices form on <111> directions, forming {110} planes and are best visualized by imaging using the [111] crystal orientation. Void superlattices have been observed in bcc metals.

Various models have been developed to explain void superlattice formation including elastic interactions of voids, spatial fluctuations of defects and anisotropic mass transport. The principle concept of the most popular anisotropic mass transport model is that voids aligned along close-packed directions shield each other from one-dimensional migrating crowdion or interstitial dumbbells [28, 29]. Under such a shadowing condition, voids located on the same line are protected by the leading voids from being diminished. For those voids not completely aligned, the non-shadowed portion of the void will disappear due to its higher likelihood to interact with interstitials. For slightly unaligned voids, they will therefore shift their centers for better alignment with interstitials. It is unclear at this stage which type of interstitial defects are responsible for void alignment. They can be crowdions, a chain of displaced interstitial-vacancy cluster, or interstitial dimers, or glissile dislocation loops.

3.5. Conclusions

We have studied swelling resistance of Cr by Fe ion irradiation over temperature range of 450-650°C. Void swelling peaks at 550°C. Compared with pure iron with a post-transient swelling rate of ~0.2%/dpa, pure chromium swells at a much lower rate of ~0.03-0.04%/dpa. Void alignment along [111] axial direction was observed. Swelling, while low in post-transient rate appears in both this and earlier studies, to begin quickly with essentially zero incubation dose, exhibiting a much higher transient swelling rate before settling onto the post-transient value. The easy swelling, in comparison with pure Fe, needs to be considered in Cr coating concept.

3.6. References

[1] J.F. Ziegler, M.D. Ziegler, J.P. Biersack, SRIM – the stopping and range of ions in matter, Nucl. Instr. Meth. Phys. Res. B 268 (2010).

[2] R.E. Stoller, et al., On the use of SRIM for computing radiation damage exposure, Nuclear Instruments and Methods in Phys. Res. B 310, 75-80 (2013).

[3] L. Shao, et al., Effect of defect imbalance on void swelling distributions produced in pure iron irradiated with 3.5 MeV self-ions, Journal of Nuclear Materials 453, 176-181 (2014).

[4] J.G. Gigax et al., The influence of ion beam rastering on the swelling of self-ion irradiated pure iron at 450 °C, Journal of Nuclear Materials 465, 343-348 (2015).

[5] F. A. Garner, "Impact of the Injected Interstitial on the Correlation of Charged Particle and Neutron-Induced Radiation Damage", J. Nucl. Mater., 117 (1983) 177-197.

[6] C. Sun, F.A. Garner, L. Shao, X. Zhang, S.A. Maloy, "Influence of injected interstitials on the void swelling in two structural variants of 304L stainless steel induced by self-ion irradiation at 500°C, Nucl. Instr. Meth. Res. B 409 (2017) 323-327.

[7] C. Sun, L. Malerba, M.J. Konstantinovic, F.A. Garner and S.A. Maloy, "Emulating Neutron-Induced Void Swelling in Stainless Steels Using Ion Irradiation", Proceedings of the 18th International Conference on Environmental Degradation of Materials in Nuclear Power Systems–Water Reactors 2017, The Minerals, Metals & Materials Series, pp. 669-680.

[8] J.G. Gigax, T. Chen, Hyosim Kim, J. Wang, L.M. Price, E. Aydogan, S.A. Maloy, D.K. Schreiber, M.B. Toloczko, F.A. Garner, Lin Shao, "Radiation response of alloy T91 at damage levels up to 1000 peak dpa", J. Nucl. Mater. 482 (2016) 257-265.

[8] E. Getto, G. Vancoevering, G. S. Was, The co-evolution of microstructure features in self-ion irradiated HT9 at very high damage levels, J. Nucl. Mater. 484 (2017) 193-208.

[10] E. Aydogan, T. Chen, J.G. Gigax, D. Chen, X. Wang, P.S. Dzhumaev, O.V. Emelyanova, M.G. Ganchenkova, B.A. Kalin, M. Leontiva-Smirnova, R.Z. Valiev, N.A. Enikeev, M.M. Abramova, Y. Wu, W.Y. Lo, Y. Yang, M. Short, S.A. Maloy, F.A. Garner, L. Shao, "Effect of self-ion irradiation on the microstructural changes of alloy EK-181 in annealed and severely deformed conditions", J. Nucl. Mater.487 (2017) 96-104.

[11] Krishan, K., “Invited review article ordering of voids and gas bubbles in radiation environments”, Radiat. Eff., 66 (1982) 121.

[12] Jäger, W. and Trinkaus, H., “Defect ordering in metals under irradiation” J. Nucl. Mater., 205 (1993) 394.

[13] N.M. Ghoniem, D. Walgraff and S.J. Zinkle, Theory and experiment of nanostructure self-organization in irradiated materials Journal of Computer-Aided Materials Design, 8: 1–38, 2002.

[14] D.J. Johnson, P.B. and Mazey, Gas-bubble superlattice formation in bcc metals, J. Nucl. Mater., 218 (1995) 273-288.

[15] V.Bryk, V.N.Voevodin, V.F.Zelenskiy, B.V.Matveenko, I.M.Nekhludov, V.K.Horenko, T.P.Chernyaeva, A.N.Rakitskiy, V.I.Trefilov, Investigation of radiation swelling of the deformed minor-alloyed Cr alloy under its irradiation at the accelerator. VANT 1981, pp. 33-38 (in Russian).

[16] F. A. Garner, Chapter 6: "Irradiation Performance of Cladding and Structural Steels in Liquid Metal Reactors," Vol. 10A of Materials Science and Technology: A Comprehensive Treatment, VCH Publishers, 1994, pp. 419-543.

[17] T. Okita, N. Sekimura, F. A. Garner, L. R. Greenwood, W. G. Wolfer and Y. Isobe, "Neutron-Induced Microstructural Evolution of Fe-15Cr-16Ni Alloys at ~ 400°C During Neutron Irradiation in the FFTF Fast Reactor", 10th International Conference on Environmental Degradation of Materials in Nuclear Power Systems – Water Reactors, 2001, issued on CD format, no page numbers.

[18] T. Okita, N. Sekimura, T. Iwai and F. A. Garner, "Investigation of the Synergistic Influence Of Irradiation Temperature and Atomic Displacement Rate on the Microstructural Evolution of Ion-Irradiated Model Austenitic Alloy Fe-15Cr-16Ni", 10th International Conference on Environmental Degradation of Materials in Nuclear Power Systems – Water Reactors, 2001, issued on CD format, no page numbers.

[19] N. Q. Lam, S. J. Rothman, R. Sizmann, Steady-state point-defect diffusion profiles in solids during irradiation, Radiat. Eff. 23 (1974) 53-59.

[20] Yu. V. Konobeev, A. V. Subbotin, V. N. Bykov, V. I. Tscherbak, Grain Boundary Void Denuded Zone in Irradiated Metals, Phys. Status Solidi A 29 (1975) K121-K124

[21] E. Napolitani, Silicon interstitial injection during dry oxidation of SiGe/Si J. Appl. Phys. 97, 036106 (2005).

[22] B. H. Sencer and F.A. Garner, "Compositional and Temperature Dependence of Void Swelling in Model Fe-Cr Base Alloys Irradiated in EBR-II", J. Nucl. Mater., 283-287 (2000) 164-168.

[23] F. A. Garner, M. B. Toloczko and B. H. Sencer, "Comparison of Swelling and Irradiation Creep Behavior of fcc-Austenitic and bcc-Ferritic/Martensitic Alloys at High Neutron Exposure", J. Nucl. Mater., 276 (2000) 123-142.

[24] F. A. Garner and J. F. Stubbins, "Saturation of Swelling in Neutron Irradiated Molybdenum and its Dependence on Irradiation Temperature and Starting Microstructural State," J. Nucl. Mater., 212-215 (1994) 1298-1302.

[25] F. A. Garner, "Recent Insights on the Swelling and Creep of Irradiated Austenitic Alloys" J. Nucl. Mater., 122-123 (1984) 459-471.

[26] F. A. Garner, H. R. Brager and K. R. Anderson, "Neutron-Induced Changes in Density and Electrical Conductivity of Copper Alloys at 16 to 98 dpa and 430ºC", J. Nucl. Mater., 179-181 (1991) 250-253.

[27] D. Chen, F. Gao, W.Y. Hu, S.Y. Hu, D. Terentyev, X. Sun, H.L. Heinisch, C.H. Henager, M.A. Khaleel, "Migration of Cr-vacancy clusters and interstitial Cr in α-Fe using the dimer method", Phy. Rev. B 81, 064101 (2010)

[28] H.L. Heinisch & B.N. Singh, "Kinetic Monte Carlo simulations of void lattice formation during irradiation", Phil. Mag. 83, 3661 (2003)

[29] S.Y. Hu, et al., "Formation mechanism of gas bubble superlattice in UMo metal fuels: Phase-field modeling investigation", J. Nucl. Mat. 479, 202 (2016)

[30] V.I. Trefilov, V.F. Zelenskiy, I.M. Nekhludov, A.N. Rakitskiy, N. Voevodin, L.S. Ozhigov, V.S. Karasev, A.P. Rudoy, V.N. Minakov, Y.V. Milman, A.S. Davidenko, Minor-alloyed Cr-based alloys, RM-8 (1991) pp. 185-194 (in Russian).

[31] V. P. Chakin, V. A. Kazakov, "Radiation resistance of minor-alloyed Cr alloys", RIAR preprint No. 7 (790), RIAR, Dimitrovgrad, (1990) in Russian.

[32] V. Bryk, V.N. Voevodin, V.F. Zelenskiy, B.V. Matveenko, I.M. Nekhludov, V.K. Horenko, T.P. Chernyaeva, A.N. Rakitskiy, V.I. Trefilov, Investigation of radiation swelling of the deformed minor-alloyed Cr alloy under its irradiation at the accelerator. VANT 1981, pp. 33-38 (in Russian).

[33] L. Shao et al., Standardization of accelerator irradiation procedures for simulation of neutron induced damage in reactor structural materials, Journal of Nuclear Materials 409, 251-254 (2017).

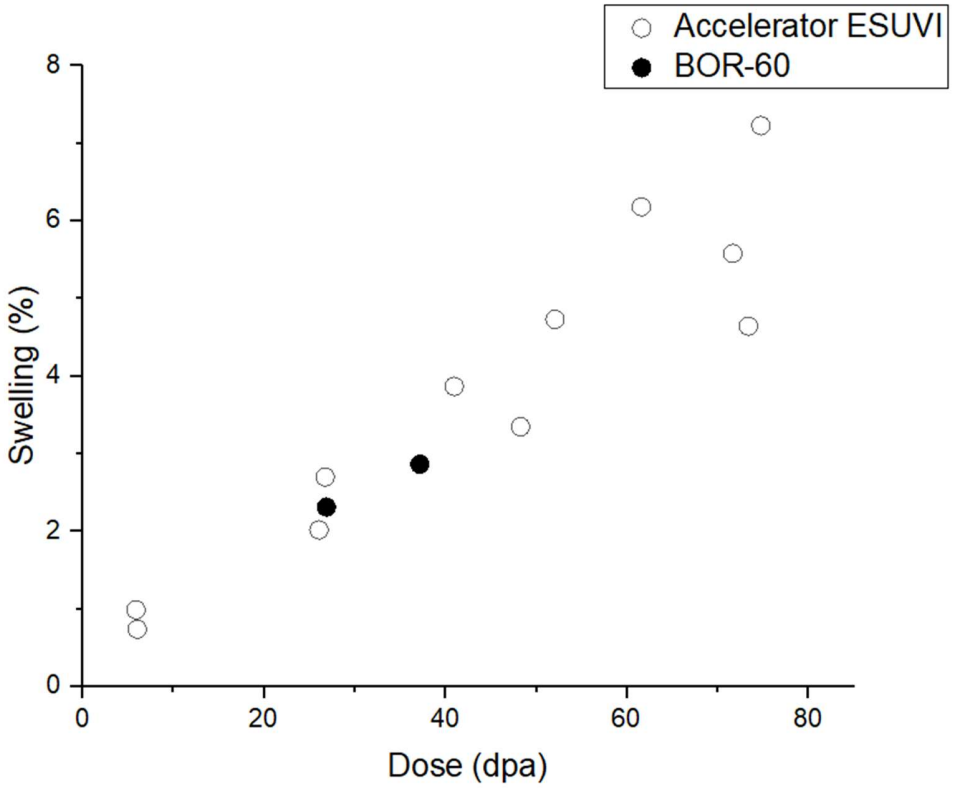

Figure A-1 Neutron-induced swelling and Cr ion-induced swelling of pure chromium over the range 650-750° C, adapted from [30]. Note that swelling starts at very low dpa levels.

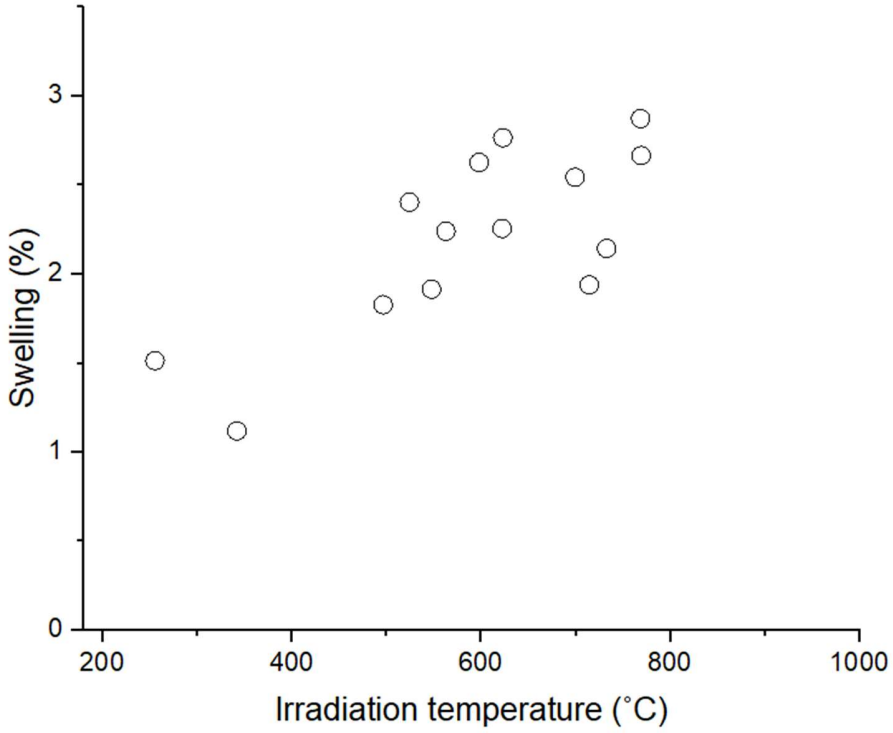

Figure A-2 Temperature dependence of swelling of chromium alloy BH-2K observed in BOR-60, adapted from [31]. The data were normalized to "constant fluence", but the method used was not specified.

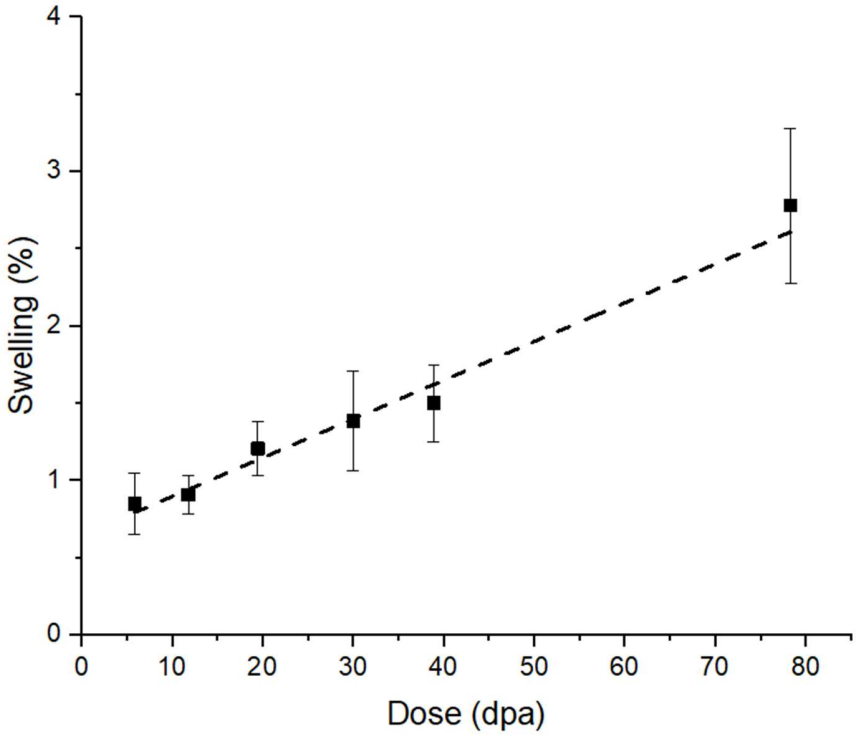

Figure A-3 Dpa dose dependence of swelling of pure chromium at 650°C, adapted from [32].